DISSOLUTION RATES OF ALLOPHANE WITH VARIABLE FE CONTENTS: IMPLICATIONS FOR AQUEOUS ALTERATION AND THE PRESERVATION OF X-RAY AMORPHOUS MATERIALS ON MARS

S. J. Ralston[a,b,*], Elisabeth M. Hausrath[a], Oliver Tschauner[a], Elizabeth Rampe[c], Tanya S. Peretyazhko[b],
Roy Christoffersen[b], Chris DeFelice[a], Hyejeong Lee[a]

[a]University of Nevada, Las Vegas, 4505 S Maryland Pkwy, Las Vegas, NV 89154, USA. [b]Jacobs, NASA Johnson Space Center, Mail Code XI3, Houston, TX 77058, USA. [c]NASA Johnson Space Center, Houston, TX 77058, USA.
*Corresponding author: S. J. Ralston, silas.ralston@nasa.gov

ABSTRACT

Recent measurements from Mars document X-ray amorphous/nano-crystalline materials in multiple locations across the planet. However, despite their prevalence, little is known about these materials or what their presence implies for the history of Mars. The X-ray amorphous component of the martian soil in Gale crater has an X-ray diffraction pattern that can be partially fit with allophane (approximately $Al_2O_3 \bullet (SiO_2)_{1.3\text{-}2} \bullet (H_2O)_{2.5\text{-}3}$), and the low-temperature water release data are consistent with allophane. The chemical data from Gale crater suggest that other silicate materials similar to allophane, such as Fe-substituted allophane (approximately $(Fe_2O_3)_{0.01\text{-}0.5}(Al_2O_3)_{0.5\text{-}0.99} \bullet (SiO_2)_2 \bullet 3H_2O$), may also be present. In order to investigate the properties of these potential poorly crystalline components of the martian soil, Fe-free allophane (Fe:Al = 0), Fe-poor allophane (Fe:Al = 1:99), and Fe-rich allophane (Fe:Al = 1:1) were synthesized and then characterized using electron microscopy and Mars-relevant techniques, including infrared spectroscopy, X-ray diffraction, and evolved gas analysis. Dissolution experiments were performed at acidic (initial pH values $pH_0 = 3.01$, $pH_0 = 5.04$), near-neutral ($pH_0 = 6.99$), and alkaline ($pH_0 = 10.4$) conditions in order to determine dissolution kinetics and alteration phases for these poorly crystalline materials. Dissolution rates (r_{diss}), based on the rate of Si release into solution, show that these poorly crystalline materials dissolve approximately an order of magnitude faster than crystalline phases with similar compositions at all pH conditions. For Fe-free allophane, $\log r_{diss} = -10.65 - 0.15 \times pH$; for Fe-poor allophane, $\log r_{diss} = -10.35 - 0.22 \times pH$; and for Fe-rich allophane, $\log r_{diss} = -11.46 - 0.042 \times pH$ at 25°C, where r_{diss} has the units of mol m^{-2} s^{-1}. The formation of incipient phyllosilicate-like phases was detected in Fe-free and Fe-rich allophane reacted in aqueous solutions with $pH_0 = 10.4$ (steady-state pH $\approx$ 8). Mars-analog instrument analyses demonstrate that Fe-free allophane, Fe-poor allophane, and Fe-rich allophane are appropriate analogs for silicate phases in the martian amorphous soil component. Therefore, similar materials on Mars must have had limited interaction with liquid water since their formation. Combined with chemical changes expected from weathering, such as phyllosilicate formation, the rapid alteration of these poorly crystalline materials may be a useful tool for evaluating the extent of aqueous alteration in returned samples of martian soils.

INTRODUCTION

Recent observations have shown that Mars likely once had abundant liquid water (e.g., Carr 1996; Bibring et al. 2006; Vaniman et al. 2014; Grotzinger et al. 2015), widely considered to be a critical prerequisite for life. However, the amount of liquid water that was present on Mars, and how long it was present, is not yet clear. Clues to the characteristics and longevity of Mars's ancient aquatic environments may lie in aqueous alteration products, including the poorly crystalline, nano-crystalline, or X-ray amorphous soil components (which we refer to as "amorphous" for simplicity) that have been detected widely on Mars from orbit (e.g., Singer 1985; Milliken et al. 2008; Rampe et al. 2012; Weitz et al. 2014) and *in situ* by the Pathfinder, Spirit, and Curiosity rovers (e.g., Morris et al. 2000; Squyres et al. 2008; Bish et al. 2013). Amorphous materials containing structural or adsorbed water may be the source of globally distributed hydrogen observed on Mars (Meslin et al. 2013). One such material, allophane (approximately $Al_2O_3•(SiO_2)_{1.3-2}•(H_2O)_{2.5-3}$), has been detected from orbit across many regions of Mars (Rampe et al. 2011; Rampe et al. 2012; Bishop and Rampe 2016), and has been proposed as a possible component of the amorphous material at Gale crater, the landing site of the Mars Science Laboratory rover Curiosity (Bish et al. 2013; Dehouck et al. 2014).

Allophane is a poorly ordered aluminosilicate that forms on Earth from the weathering of volcanic rocks and ash in moist, temperate climates (e.g., Wada 1989; Parfitt 1990; Gustafsson et al. 1998). Allophane has short-range atomic order and forms aggregates of hollow, porous nano-scale spherules approximately 50 Å in diameter (Abidin et al. 2004), giving it a large adsorption capacity and a high surface area (Ohashi et al. 2002; Iyoda et al. 2012). Allophanes can have a range of Al:Si ratios, and at Al:Si ratios below ~2:1, the "excess" Si is polymerized in the interior of the allophane nano-spherules (Childs et al. 1990; Parfitt 1990). In Fe-rich soils, Fe^{3+} can isomorphically substitute for some or most of the Al, producing Fe-substituted allophane (e.g., Kitagawa 1973) or a related mineral, hisingerite (approximately $Fe^{3+}_2Si_2O_5(OH)_4•H_2O$, Henmi et al. 1980). Like allophane, hisingerite is poorly ordered and tends to form aggregates of hollow, porous nano-spherules in soils (Ingles and Willoughby 1967), although the nano-spherules are much larger (~200 Å in diameter as per Shayan 1984).

Measurements from the Chemistry and Mineralogy (CheMin) instrument aboard Curiosity indicate that amorphous material is present in abundances from ~15-70 wt.% in all samples measured to date (e.g., Bish et al. 2013; Blake et al. 2013; Dehouck et al. 2014; Vaniman et al. 2014; Treiman et al. 2016; Rampe et al. 2017; Sutter et al. 2017). The broad hump in the CheMin X-ray diffraction (XRD) patterns of these samples, which was assigned to amorphous material, has been fit by a combination of allophane, ferrihydrite, and/or rhyolitic and basaltic glass for samples of modern aeolian sediment (e.g., the Rocknest aeolian bedform; Bish et al. 2013; Achilles et al. 2017) and ancient sandstone and mudstone (e.g., the Cumberland, John Klein, and Windjana drill sites; Vaniman et al. 2014; Treiman et al. 2016; Rampe et al. 2017). Plausible chemical composition of the amorphous component for inactive aeolian sediment (i.e., soil) was estimated by subtracting the calculated composition of the crystalline component (determined from CheMin data) from the bulk sample composition obtained from Curiosity's Alpha Particle X-Ray Spectrometer (APXS) (Bish et al. 2013; Dehouck et al. 2014; Vaniman et al. 2014). Based on the Fe-rich nature of the material, hisingerite may be present instead of or in addition to allophane (Bish et al. 2013; Dehouck et al. 2014).

Weathering of basaltic materials on Mars could have produced amorphous silica and Al-rich clay minerals if the water-rock ratio was high (e.g., Catalano 2013). Amorphous silica and Al-rich clay minerals on Mars may represent the final stages of an alteration sequence in which allophane is an intermediate product. Although much research has been done on the structure of allophane (e.g., Childs et al. 1990; Ohashi et al. 2002; Montarges-Pelletier et al. 2005; Iyoda et al. 2012; Bishop et al. 2013), few data exist on its alteration mechanisms, including dissolution kinetics (Abidin et al. 2004), and to our knowledge no dissolution rates have been measured for Fe-rich allophane.

The objectives of this study were to determine the rates and conditions under which analogs for the martian amorphous soil component persist, dissolve, and form secondary alteration phases. Fe-free allophane, Fe-poor allophane, and Fe-rich allophane were synthesized; batch dissolution experiments of these phases were performed in acidic, near-neutral, and alkaline conditions; and the altered materials were characterized. The obtained results can help to place constraints on the characteristics and longevity of liquid water that was present in allophane-bearing regions on Mars after the formation of these amorphous materials and to search for direct evidence of past aqueous alteration in returned martian samples.

MATERIALS AND METHODS

Synthesis procedures

Fe-free allophane, Fe-poor allophane, and Fe-rich allophane were synthesized following the methods of Baker and Strawn (2012, 2014) and Baker et al. (2014). Plastic labware was used for all steps of the synthesis in order to avoid silica contamination from glass.

Syntheses were carried out using $AlCl_3 \bullet 6H_2O$ (reagent grade, Alfa Aesar, Haverkill, MA, USA), $FeCl_3 \bullet 6H_2O$ (ACS grade, Mallinckrodt, Staines-upon-Thames, United Kingdom), and tetraethyl orthosilicate (TEOS) (≥98% purity, Acros Organics, Fair Lawn, NJ, USA). Solutions of 0.1 M $AlCl_3$ and $FeCl_3$ were mixed, and TEOS was added. While stirring, a solution of 1 M NaOH (reagent grade, VWR Chemicals BDH, Poole, United Kingdom) was added to the solution with a variable speed Just Infusion syringe pump (Model NE-300, New Era Pump Systems Inc., East Farmingdale, NY, USA) at a rate of 25 mL h^{-1} in order to hydrolyze TEOS and allow Si to bond with Al and Fe. The NaOH solution was added until a molar ratio of OH/(Al+Fe) = 3:1 was achieved in order to maximize allophane production and minimize the production of other phases, such as imogolite (Denaix 1993). The recipes used for synthesis of Fe-free allophane, Fe-poor allophane, and Fe-rich allophane, along with the Al:Fe:Si molar ratio, Brunauer-Emmett Teller (BET) specific surface area (SSA) and average particle size of each unaltered material, are summarized in **Table 1**. The precursor materials were stirred for one additional hour after NaOH addition to ensure thorough mixing, and then incubated without stirring at room temperature overnight to stabilize the suspension through an initial stage of colloid formation and proton release (Denaix 1993; Montarges-Pelletier et al. 2005). The precursors were then heated in an oven at 95ºC for seven days to promote colloid growth and maturation. The samples were removed from the oven, cooled on the lab bench to room temperature, and washed with 18.2 MΩ deionized water until the conductivity of the supernatant was <20 µS to remove excess ions and alcohol from TEOS. The washed products were frozen in a -20ºC freezer for at least 24 hours, and then freeze-dried to create the final solid product. Samples were sieved to <355 µm prior to use in dissolution experiments.

Characterization of unaltered material

The synthesized Fe-free allophane, Fe-poor allophane, and Fe-rich allophane were characterized by Fourier-transform infrared photoacoustic spectroscopy (FTIR-PAS), X-ray diffraction (XRD), evolved gas analysis (EGA), scanning electron microscopy/energy dispersive X-ray spectroscopy (SEM/EDS), field-emission SEM (FE-SEM), field-emission scanning transmission electron microscopy (FE-STEM), BET SSA analysis, particle size analysis, and total chemistry by total digestion.

FTIR-PAS FTIR-PAS analyses were carried out on a Varian FTS 7000 FTIR spectrometer with a photoacoustic detector (Varian Inc., Palo Alto, CA, USA) in the Inorganic Materials & Nanomaterials lab at the University of Nevada, Las Vegas (UNLV). The use of photoacoustic techniques allowed samples to be analyzed with minimal preparation and was non-destructive to the sample. Absorption spectra were obtained on loosely packed powdered samples. For all runs, the scanning speed was 2.5 kHz, with 64 scans collected at a resolution of 4 cm^{-1} over the 4,000-400 cm^{-1} (2.5-25 µm) range. For each sample, the sample chamber with the sample was run through an open helium purge for 10 min, followed by a closed helium purge for another 10 min in order to minimize contamination from atmospheric gases. Carbon black was used to obtain a background spectrum for each run, and this background spectrum was used as a correction for all sample spectra in order to remove absorptions due to CO_2 and other atmospheric gases.

XRD XRD patterns for unreacted Fe-free allophane, Fe-poor allophane, and Fe-rich allophane were obtained using a PANalytical X'Pert Pro MPD 3040 instrument (Malvern Panalytical Ltd., Malvern, United Kingdom) with a traditional spinner stage at NASA Johnson Space Center. Co Kα radiation was used for all samples for comparison to CheMin XRD data. The scans were conducted at 45 kV/40 mA, from 2º to 80º 2θ with a step size of 0.02º 2θ, 100 seconds per step. Before analysis, samples were crushed gently in an agate mortar and pestle to break up aggregates and sieved to <75 μm. Silicon zero-background slides in aluminum sample holders were used for all samples.

EGA Evolved gas analysis was conducted on Fe-free allophane, Fe-poor allophane, and Fe-rich allophane in order to compare these synthetic materials with those measured in Gale crater by the Sample Analysis at Mars (SAM) instrument on the Curiosity rover. EGA was conducted under conditions similar to those utilized by SAM (i.e., ramp rate, pressure, and carrier gas). The analyses were conducted in a Setaram LabSys Evo thermal gravimeter/differential scanning calorimeter (TG/DSC) furnace (Setaram Inc., Caluire, France) coupled to a Pfeiffer ThermoStar GSD 320 quadrupole mass spectrometer (Pfeiffer Vacuum, Aßlar, Germany) at NASA Johnson Space Center. The temperature range was from 30ºC to 1,000ºC with a ramp rate of 35ºC min^{-1}. The carrier gas was helium, with a flow rate of 10 mL min^{-1}, and the pressure was 30 mbar. Approximately 10 mg of sample was used for each run, and samples were run in duplicate.

Microscopy Freeze-dried aggregates of unaltered Fe-free allophane, Fe-poor allophane, and Fe-rich allophane were placed on carbon tape atop aluminum sample plugs and carbon coated for analysis using a Denton Vacuum DV-502A carbon coater (Denton Vacuum LLC, Moorestown, NJ, USA). SEM and EDS analyses were carried out on a JEOL scanning electron microscope model JSM-5600 (JEOL Ltd., Akishima, Tokyo, Japan) with a magnification range of 35x to 100,000x (1 µm resolution) with an Oxford ISIS EDS system (Oxford Instruments, Abingdon, United Kingdom) in the Electron Microanalysis and Imaging Laboratory (EMiL) at UNLV.

In order to reach sufficient magnifications to distinguish the nano-spherules characteristic of allophane, samples were examined on a JEOL JSM-6700F field-emission SEM (JEOL Ltd., Akishima, Tokyo, Japan) with a magnification range of 500x to 430,000x (5 µm to 10 nm resolution) in the EMiL at UNLV. Sample preparation was the same as for SEM/EDS analyses. A standard voltage of 15 kV was used, with a working distance of 8.4 ± 0.1 mm. Fe-free allophane was examined in secondary electron mode to investigate topography of particles, whereas Fe-poor and Fe-rich allophane were examined in backscatter mode to investigate potential chemical variations within and between particles.

Transmission electron microscopy was carried out using a JEOL JEM-2500SE analytical field-emission scanning transmission electron microscope (FE-STEM) (JEOL Ltd., Akishima, Tokyo, Japan) with up to 1,000,000x magnification (1.5 nm resolution) at NASA Johnson Space Center. Both conventional and STEM bright-field imaging were used in order to identify major morphological features of the grains, such as nano-spherules. Assessment of features on the crystal structure scale, including those indicative of short- or long-range atomic order, was made using high-resolution lattice fringe imaging (HRTEM). Freeze-dried samples were gently crushed in an agate mortar and pestle to break up aggregates, suspended in ethanol, and droplet-deposited on amorphous holey-carbon films supported on 200 mesh transmission electron microscope (TEM) grids (Electron Microscopy Sciences, Hatfield, PA, USA). Major element composition of grains was assessed by EDS.

BET surface area and particle size analysis Approximately 400 mg each of unreacted, unground synthetic Fe-free allophane, Fe-poor allophane, and Fe-rich allophane, sieved to the <355 µm size fraction used in the dissolution experiments, were prepared for determination of BET SSA and particle size analysis. The BET SSA values were used to normalize the calculated dissolution rates to surface area and allow comparison of calculated rates to the literature. BET SSA was determined using a Micromeritics TriStar II 3020 surface area and porosity instrument (Micromeritics Instrument Corporation, Norcross, GA, USA) at NASA Johnson Space Center. N_2 was used as the analysis adsorptive. Samples were degassed at 250°C under vacuum overnight to remove adsorbed water, which can interfere with accurate BET results by occupying adsorption sites and preventing the analysis adsorptive from adsorbing. This temperature was chosen because it exceeds the temperature of water release for allophane (100-150°C, Bish and Duffy 1990; Rampe et al. 2016) but is well below the temperature at which allophane begins to transform to mullite (900-950°C, Parfitt 1990). Particle size analysis was conducted on a Microtrac Bluewave S4640 particle size analyzer (MicrotracBEL, Osaka, Japan) at NASA Johnson Space Center. Samples were dispersed in ethanol and sonicated prior to analysis. All analyses were run in duplicate to allow estimates of uncertainty.

Total chemistry Digestions were performed following a modification of the method of Potts et al. (1984) in order to quantify changes in chemical composition due to alteration. For each sample, approximately 0.1 g of material was mixed in a 1:5 mass ratio with lithium tetraborate (≥98%, Acros Organics, Fair Lawn, NJ, USA). The dry mixture was heated at 975°C in a graphite crucible for 20 min, and then allowed to cool to room temperature. The melt bead was removed from the crucible, mixed with 100 mL of 1 M HNO_3 (Mallinkcrodt, Staines-upon-Thames, United Kingdom) and stirred for 1 h on low heat (~40°C). Another 100 mL of 1 M HNO_3 was added after 1 h, and the suspension was stirred for an additional 1 h on low heat until the melt bead fully dissolved. The solution was stirred at room temperature overnight to ensure complete dissolution of silica species. After the overnight stirring step, an aliquot of the solution was filtered to 0.2 μm and sent to UNLV for Al-Si-Fe measurements using an iCAP Qc Inductively Coupled Plasma Mass Spectrometer (ICP-MS) (Thermo Scientific, Waltham, MA, USA). Graphite residues were observed on the filters due to graphite coatings on the original melt beads, but no other residues (i.e., incompletely dissolved sample) were observed on the filters. Filtered sample solutions were diluted by a factor of 100 for Si-Fe measurements, and by a factor of 1,000 for Al measurements. Synthetic multi-element standard solutions were made from HPS™ single element standard solutions (High Purity Standards, North Charleston, SC, USA) and were used to construct standard calibration curves. The peaks of ^{27}Al, ^{28}Si, ^{29}Si, and ^{57}Fe were monitored under kinetic energy discrimination (KED) mode with collision cell gas on to remove molecular interferences. The blank correction was typically lower than 15% for Si, 6% for Fe, and 1% for Al. The sensitivity drift within each analytical sequence was less than 15%, and it was corrected by using an external drift monitor (e.g., DeFelice et al. 2019). Each solution was measured twice in two analytical sequences. These two measurements agreed within ± 3%, and their averages were reported.

Dissolution experiments and solution chemistry analysis

Experiments were prepared by adding 150.0 ± 0.4 mg of sample (Fe-free allophane, Fe-poor allophane, or Fe-rich allophane, sieved to <355 μm) in acid-washed 250 mL polypropylene bottles containing 180 mL of 0.01 M NaCl solution (made with reagent grade NaCl, VWR Chemicals BDH, Poole, United Kingdom) adjusted to pH 3, 5, 7, or 10.4. The bottles were shaken in a shaker water bath at 25.0 ± 0.1°C at 50 rpm. The pH was adjusted with high-purity concentrated HNO_3 or NaOH. Experiments were performed in batch to examine changes in the solid material at steady-state conditions, such as formation of incipient phyllosilicates, likely relevant to low water-to-rock (W/R) ratio isochemical reactions that may have occurred on Mars. The pH was not buffered due to the potential for changes in reaction rate and mechanism caused by the presence of buffers in solution (e.g., Dove and Crerar 1990; Wogelius and Walther 1991; Stillings and Brantley 1995). However, 0.01 M NaCl solution was used instead of deionized water to reduce drastic changes in ionic strength due to dissolution, which can significantly affect the dissolution rates of high-silica materials compared to dissolution in pure water (Dove and Nix 1997; Icenhower and Dove 2000). Each experiment was run in duplicate with one blank at each pH condition. Blanks consisted of 0.01 M NaCl solution with no added allophane, with the same amount of HNO_3 or NaOH added as in the experiments. Solution aliquots (10 mL each) were taken periodically based on expected dissolution rates of similar materials (e.g., Liang and Readey 1987; Icenhower and Dove 2000; Huertas et al. 2001; Gislason and Oelkers 2003; Abidin et al. 2004; Rozalen et al. 2008; Gainey et al. 2014; Steiner et al. 2016) and preliminary experiments. The resulting change in water-sample ratio was corrected for when calculating the elemental release rate (see *Calculations* below). The first 8 mL of each sample aliquot was filtered through a 0.2 μm filter and acidified with 1% v/v high purity HNO_3 (67-70%, VWR Chemicals BDH, Poole, United Kingdom). The pH of the solution was measured from the remaining 2 mL of unfiltered sample aliquot. Dissolution experiments are summarized in **Table 2**, and the full experimental conditions for each experiment, including initial and final pH and total reaction time, are given in the supplemental material (**Data Sheets S1-S38**). Experiments are referred to by starting pH (pH_0) and material: Fe-free allophane (FFA), Fe-poor allophane (FPA), or Fe-rich allophane (FRA). For example, a dissolution experiment with Fe-free allophane with an initial pH of 3 would be named "pH_0_3_FFA."

Elemental analyses for dissolved Fe, Al, and Si were conducted via flame atomic absorption (AA) spectroscopy on a Thermo Scientific iCE 3000 Series AA Spectrometer (Thermo Scientific, Waltham, MA, USA) at UNLV. Dissolved Fe was measured using an air-acetylene flame and had a practical quantitation limit of 0.2 mg L^{-1}. The practical quantitation limit is defined as the concentration at which the instrument response is roughly 10 times greater than the standard deviation of the calibration (Gibbons et al. 1991). Dissolved Al and Si were measured using an air-acetylene-nitrous oxide flame and had practical quantitation limits of 1.0 mg L^{-1} and 0.2 mg L^{-1} respectively. Fe samples were treated with $CaCO_3$ (ACS grade, RICCA Chemical Company, Arlington, TX, USA) to reduce interference, and Al samples were treated with KCl (molecular biology grade, EMD Millipore, Burlington, MA, USA) to control ionization, following the methods of Eaton et al. (2005), and 18.2

MΩ deionized water was used as an instrument blank.

Calculations

Dissolution rates were determined from moles Si released into solution with time. The Si concentration measured in solution was corrected for volume removed during sampling to obtain moles Si released using the equation:

$$m_t = m_{(t-1)} + \left(c_t - c_{(t-1)}\right) V_{(t-1)} \qquad (1)$$

where m_t and $m_{(t\text{-}1)}$ are the moles Si released at times t and t-1, c_t and $c_{(t\text{-}1)}$ are the corresponding concentrations (mol L^{-1}), and $V_{(t\text{-}1)}$ is the volume of solution (L) remaining at time t-1 (Welch and Ulmann 2000). Dissolution of all materials showed an initial linear rapid Si release phase, followed by a slower phase that approaches steady conditions (**Fig. 1**). This approach to steady conditions is expected in batch (closed-system) conditions either due to equal rates of silica dissolution from one phase and silica precipitation to another phase, or due to true chemical equilibrium with respect to some silica-containing phase. The initial linear part of the curve was determined by fitting a preliminary regression line through the Si release data for the first 7 h of the experiment (generally equivalent to the first 3-4 points), and the last data point that was within two standard deviations (2σ) of this line was considered the final point of the linear part of the curve. This approach is similar to the method used by Abidin et al. (2004) to determine the point at which allophane dissolution transitions from an initial, rapid rate to a slower rate approaching steady-state. The section of the Si release curve between zero and the first time point was not included in these calculations, as it may represent release of Si due to rapid dissolution of fine particles (e.g., Nagy et al. 1991), and would therefore not be representative of the dissolution rate of the bulk material. When the first point had a higher silica concentration than the second point (both replicates of pH_0_5_FRA, one replicate each of pH_0_5_FFA and pH_0_5_FPA), the first point was not included in the regression, as this was interpreted as inadvertent sampling of solid material. The initial linear part of the Si release curve determined as described above was then fit with a linear regression, where the slope of the line was the silica release rate in mol s^{-1}. The dissolution rate was calculated using the following equation:

$$r_{diss} = \frac{\Delta m / \Delta t}{A \times M} \qquad (2)$$

where r_{diss} is the dissolution rate (mol m^{-2} s^{-1}), $\Delta m/\Delta t$ is the silica release rate (mol s^{-1}), A is the average initial BET SSA of the material (m^2 g^{-1}), and M is the total mass of material in the reactor (g) (**Table 3**). One of the duplicate experiments of pH_0_7_FPA was excluded from the rate calculations due to anomalous experimental conditions (see **Data Sheet S18**, supplemental material). Although BET surface area is not a perfect measurement of reactive surface area (e.g., Velbel 1993; Gautier et al. 2001; Sanders et al. 2012), it allows comparisons of these surface area-normalized dissolution rates to surface area-normalized measurements in the literature.. The average pH of the linear section of the dissolution curve was considered to be the pH of the experiment, since the dissolution rate is also determined over the same section (see *Solution chemistry* and Section S10).

Rate laws were determined by plotting the log of the dissolution rates from Equation *(2)* against the pH of the experiment, and then fitting the points with a linear regression. The resulting rate law was of the form:

$$\log r_{diss} = \log k_{diss} - n \times pH \qquad (3)$$

where k_{diss} is the dissolution rate constant, and n is the reaction order with respect to H^+.

In order to provide a comparison to studies of other rapidly dissolving phases (e.g., Elwood-Madden et al. 2012; Miller et al. 2016), particle lifetimes of Fe-free allophane, Fe-poor allophane, and Fe-rich allophane were calculated by the shrinking sphere model (Lasaga 1984):

$$t = \frac{d}{2 r_{diss} V_m} \qquad (4)$$

where t is the particle lifetime (s), d is the particle diameter (m), r_{diss} is the dissolution rate (mol m^{-2} s^{-1}) from *Eq. (3)*, and V_m is the molar volume (m^3 mol^{-1}). The molar volume of all allophane samples was assumed to be ~101 cm^3 mol^{-1} based on density values from Wada (1989) and calculated molecular mass because significant volume change is not expected due to Fe-substitution in allophanes (Baker et al. 2014). The particle lifetime was calculated for a particle 1 μm in diameter to facilitate comparison with similar studies (e.g., Elwood-Madden et al. 2012; Miller et al. 2016), and for the measured particle sizes of allophane aggregates in this study (given in **Table 1**). This calculation is presented as a first-order estimate of allophane particle lifetimes because allophane does not typically form solid, spherical particles in nature.

Characterization of reacted materials

Following dissolution experiments, the solution was decanted from the dissolution vessels and the solid material was centrifuged at 11,000 rpm for 5 min, washed twice with deionized water to remove excess NaCl, and then frozen for at least 24 h before freeze-drying for analysis by SEM, FE-STEM, XRD, and total digestion. The same sample preparation techniques and the same analytical conditions were used for altered material as for the unreacted material. A summary of characterizations is given in **Table 4**.

RESULTS

Characterization of unreacted materials

FTIR-PAS Infrared absorbance spectra for Fe-free allophane, Fe-poor allophane, and Fe-rich allophane (**Fig. 2a**) were similar to each other and consistent with previously published results (e.g., Wada 1989; Montarges-Pelletier et al. 2005; Rampe et al. 2012; Bishop et al. 2013; Milliken and Bish 2014). All samples had absorption bands at 3400 cm^{-1}, 1645 cm^{-1}, 1030 cm^{-1}, and 940 cm^{-1}, and a weak band near 620 cm^{-1}, and varied from the literature values by less than 50 cm^{-1} (**Fig. S1**). A full description of absorption bands and their assignments is presented in the supplemental material (Section S1).

XRD Unreacted Fe-free allophane, Fe-poor allophane, and Fe-rich allophane had similar diffraction patterns with elevated low-angle background and broad peaks (**Fig. 2b**, supplemental material **Fig. S2**), indicating an abundance of small particles and nano-crystalline structure, respectively (van der Gaast and Vaars 1981). These synthetic materials have XRD patterns consistent with previous measurements of allophane and Fe-substituted allophane. The peak positions obtained by XRD for unreacted synthesized Fe-free allophane, Fe-poor allophane, and Fe-rich allophane are presented in **Table 5** along with literature values for natural and synthetic allophane samples and natural hisingerite samples. Mustoe (1996) presents a similar summary of the d-spacings of various natural hisingerite samples from many locations, indicating variations in d-spacings of up to 0.3 Å, as well as variability in the number of observed peaks. Values for hisingerite are included as a proxy for Fe-rich allophane, as little literature exists on Fe-rich allophane (Ossaka et al. 1971; Farmer 1997; Baker and Strawn 2014).

EGA Fe-free allophane, Fe-poor allophane, and Fe-rich allophane exhibited a sharp H_2O release centered at ~130°C, likely due to release of adsorbed H_2O (**Fig. S3**), followed by a broader release from ~130-400°C which may be due to release of structural H_2O, consistent with previous laboratory measurements of water release from allophane (e.g., Bish and Duffy 1990). Release of O_2 occurred concurrently with H_2O release in all samples (**Fig. S3-S4**), indicating the O_2 production resulted from fragmentation of H_2O during ionization in the mass spectrometer. Overall, these observations are consistent with previous EGA measurements for allophane (e.g., Bish and Duffy 1990; Rampe et al. 2016). Differential scanning calorimetry (DSC) performed concurrently with EGA agreed well with differential thermal analysis (DTA) of Fe-substituted allophanes by Ossaka et al. (1971), with a peak at 960 ± 10°C for Fe-free allophane that broadened and shifted to lower temperature with increasing Fe content (924 ± 1°C for Fe-poor allophane and 791 ± 1°C for Fe-rich allophane; **Fig. S5**).

Microscopy In general, unreacted samples examined by SEM consisted of large, smooth grains ~300-600 μm across coated with much smaller (~10-50 μm) flakes of “fluffy” material (**Fig. 3a** and **S6**).

Semi-quantitative EDS analyses, conducted concurrently with SEM investigations, yielded mainly Al, Si, and Fe compositions consistent with synthesis ratios, and no major compositional differences were observed between the larger, smooth grains and the smaller, “fluffy” material (**Table S1**). FE-SEM analyses of unreacted material also showed that all samples contained small, “fluffy” aggregates (e.g., **Fig. 3b** and **S7**) as well as large chunks of material that are likely aggregates formed during centrifugation due to the rapid rotation speed (11,000 rpm) required to pull fine particles out of suspension. Chloride was detected in a few samples, most likely the result of incomplete washing, but was not prevalent (**Table S1**).

Particles with nano-spherule structures, indicative of allophane, were observed in the FE-STEM subsamples of the unreacted synthetic materials (**Fig. 4**). Nano-spherules have previously been observed in samples of natural allophane (e.g., Wada 1989; Iyoda 2012) and natural hisingerite (e.g., Eggleton and Tilley 1998). The majority of Fe-rich allophane material was structurally disordered (i.e., amorphous) based on HRTEM images analyzed by Fourier-transform image processing (**Fig. 4b**). Some synthetic Fe-rich allophane particles exhibited poorly developed lattice fringes in localized regions (e.g., **Fig. 4c**), indicative of mid- to long-range order. However, synthetic Fe-free allophane did not show any lattice fringes, even when exposed to the electron beam for several minutes (**Fig. 4e**-**f**). Two different textures were also observed in the Fe-free allophane sample; one “rugged” and one “blobby” (e.g., **Fig. 4d**). A similar textural dichotomy has previously been observed in hisingerite-like, poorly crystalline Si-Fe materials (e.g., Decarreau et al. 1987). Based on observations of a similar texture in the altered Fe-free allophane, the “blobby” texture is likely more hydrated than the “rugged” texture. Only the “rugged” texture was observed in the Fe-rich allophane. These morphologies are consistent with those presented by Wada (1989) for natural allophane and Eggleton and Tilley (1998) for natural hisingerite.

BET surface area and particle size analysis The average BET SSA and particle sizes for unaltered Fe-free allophane, Fe-poor allophane, and Fe-rich allophane are given in **Table 1**. The average BET SSA for each material was used to normalize the initial dissolution rates to surface area. However, BET surface area is not a perfect measurement of reactive surface area (Velbel 1993; Gautier et al. 2001), especially in the case of materials with large internal surface areas, such as allophane. Additionally, due to the tendency for allophane to form large aggregates consisting of hollow, porous nano-spheres (e.g., **Fig. 3**; Abidin et al. 2004), the particle sizes reported here represent the mean sizes of aggregate "grains" of each material, which helps to explain the apparent discrepancy between large particle sizes and high surface areas. The complete results of particle size analyses and BET SSA analyses are given in the supplemental material (**Table S2**).

Total digestions Comparison of digestion data with predicted compositions of the unaltered materials from the formulae indicates additional water present in the synthesized phases, either structural or adsorbed, as well as the phases potentially being enriched in Al (**Table 6**). The compositions of synthetic Fe-free allophane and Fe-poor allophane are similar to some natural samples, and synthetic Fe-rich allophane is similar to certain synthetic hisingerite used in other studies (e.g., Baker and Strawn 2014), although it is more Al-rich than most natural hisingerite samples and the Mars amorphous component, and more Fe-rich than most natural allophane samples (**Tables 4** and **S3-S6**).

Dissolution experiments

Solution chemistry For all experiments, an initial rapid linear change in pH occurred (**Fig. 5**), which then leveled off to a steady pH value (pH_{steady}), corresponding to a stage in which a lack of change in solution chemistry was observed (**Fig. S8**, **Data Sheets S1-S38**). The average pH of the linear release stage was calculated and used as the pH of the experiment for calculation of the rate constant (see *Calculations*). The initial and final pH data for the linear release stage of dissolution are summarized in **Table 3**.

The production or consumption of H^+ during dissolution of Fe-free allophane, Fe-poor allophane, and Fe-rich allophane can explain the observed pH trends, as well as the potential for formation of secondary phases. For example, the dissolution of Fe-free allophane at pH_0 3 is described by the reaction

$$(Al_2O_3)(SiO_2)_2\cdot 3H_2O+6H^{+\text{¿}}\rightarrow 2Al^{3+\text{¿}+2H_4SiO_4+2H_2O\text{¿}}\text{¿} \qquad (5)$$

where H^+ ions are consumed, driving the increase in pH with time observed in the pH_0_3_FFA experiment. At pH_0 10, the dissolution of Fe-free allophane is described by the reaction

$$(Al_2O_3)(SiO_2)_2\cdot 3H_2O+6H_2O\rightarrow 2Al(OH)_4^{-\text{¿}+2H_3SiO_4^{-\text{¿}+4H^{+\text{¿¿}}\text{¿}}\text{¿}} \qquad (6)$$

where H^+ ions are produced, driving the decrease in pH with time observed in the pH_0_10_FFA experiment. The relationship between predicted production and consumption of H^+ ions and observed changes in pH in these experiments was consistent across the range of pH conditions studied (supplemental material, Section S8). Although dissolution was not stoichiometric, the general trends described by the equations held true; namely, that the predicted production and uptake of H^+ ions during Fe-rich allophane dissolution was less than that predicted during Fe-free allophane and Fe-poor allophane dissolution. The scatter in the experimental rate data was likely due to the small dependence of silica release rate on pH and possibly also due to pH change during the experiments (**Fig. 5** and **S8**).

Fe remained below the practical quantitation limit of the atomic absorption spectrometer (<0.2 mg L^{-1}) throughout the duration of the experiment in all experiments except pH_0_3_FRA. Iron concentration in solution in the pH_0_3_FRA experiment first increased rapidly, then decreased more slowly (**Fig. 1a** and **S9**). Likewise, Al was only above the practical quantitation limit (1.0 mg L^{-1}) in the pH_0 3 experiments, likely because these were the only experiments whose pH remained below ~5 for the duration of the experiment, and Al precipitation is expected near or above pH ~5. Al concentration in the pH_0 3 experiments first rose rapidly, and then leveled off or decreased slowly as the pH approached pH_{steady}, similar to the behavior of Fe in these solutions (**Fig. 1a** and **S10**).

For all experiments, Si concentrations were above the practical quantitation limit (0.2 mg L^{-1}) at all time points (**Fig. 1a** and **S11-S14**), and changes in Si concentrations were similar to trends in pH. Initially, dissolved Si concentrations increased linearly (e.g., **Fig. 1b**), and then gradually leveled off to steady concentrations of ~0.2-0.5 mM within 18 days.

Dissolution of Fe-free allophane, Fe-poor allophane, and Fe-rich allophane was non-stoichiometric at pH_0 3. During the pH_0_3_FRA experiment, Fe release was always below the ~0.5:1 stoichiometric formula Fe/Si ratio, while Al release was initially higher than the ~0.5:1 stoichiometric formula Al/Si ratio, and then decreased with time to approximately stoichiometric formula values (**Fig. 6**). The pH_0_3_FFA and pH_0_3_FPA experiments also showed Al/Si ratios in solution that were initially above stoichiometric formula values and then decreased to below the ~1:1 stoichiometric formula value (**Fig. 6**). Determination of whether dissolution at pH_0 5, 7, and 10 was stoichiometric was not possible because dissolved Fe and Al remained below the practical quantitation limit of the AA spectrometer throughout these experiments; low concentrations in solution could have been due to precipitation of secondary phases or adsorption of Fe^{3+} and Al^{3+} onto surfaces. Solution chemistry for each time point for each experiment is reported in the supplemental material (Section S10).

Rate laws Surface area-normalized dissolution rate laws (*r_{diss}, Eq. (3))* were $\log r_{diss} = -10.65 - 0.15 \times pH$ for Fe-free allophane, $\log r_{diss} = -10.35 - 0.22 \times pH$ for Fe-poor allophane, and $\log r_{diss} = -11.46 - 0.042 \times pH$ for Fe-rich allophane. Rate laws for each material were plotted along with the measured rate for each experiment (**Fig. 7**). The pH dependence for all materials was low; for Fe-free allophane, $n = 0.146 \pm 0.026$; for Fe-poor allophane, $n = 0.222 \pm 0.040$; and for Fe-rich allophane, $n = 0.042 \pm 0.016$, where the error is the 1-σ standard deviation of n. The pH dependence of Fe-free allophane and Fe-poor allophane dissolution were almost the same within uncertainty, which is not surprising given the structural and compositional similarity of these phases.

The pH dependence of Fe-rich allophane dissolution was lower than that of the Fe-free allophane and Fe-poor allophane. Similar trends in the pH-dependence of dissolution are observed for Al-rich montmorillonite (e.g., Huertas et al. 2001; Rozalen et al. 2008) and Fe^{3+}-rich nontronite (e.g., Gainey et al. 2014), and amorphous Al- and Fe^{3+}-phosphates (Tu et al. 2014), with the Fe-rich material showing a lower pH dependence than the Al-rich material in both cases. Although the water exchange rate around Fe has been shown to be more rapid than that around Al (e.g., Helm and Merbach 2005; Miller et al. 2016), the first hydrolysis constant for Fe^{3+} is much larger than that of Al^{3+} (Lamb and Jacques 1938; Frink and Peech 1963), which may result in the rapid formation of Fe-hydroxides (e.g., Hsu 1976). Additionally, precipitation of Fe-oxide or oxyhydroxide coatings on material surfaces may protect those surfaces from the surrounding solution and therefore slow dissolution of Fe-rich materials compared to Al-rich materials under acidic conditions.

Particle lifetimes Particle lifetimes for Fe-free allophane, Fe-poor allophane, and Fe-rich allophane are given in **Table 7**. Particle lifetimes were calculated both for a 1 μm particle for comparison to literature on other rapidly dissolving phases (e.g., Elwood-Madden et al. 2012; Miller et al. 2016) and using the measured particle size of each unaltered material (**Table 1**). Particle lifetimes are 0.02-0.18 kyr for a 1 μm particle, and 2.5-24.0 kyr for the measured particle sizes. Field dissolution rates of silicate minerals are generally ~2 orders of magnitude slower than laboratory dissolution rates (e.g., Velbel 1993; Zhu et al. 2016), giving a final estimate between 1.9-6.7 kyr for the lifetime of a 1 μm allophane particle in moderately acidic waters, and 10.6-18.0 kyr in moderately alkaline waters, consistent with other estimates of the lifetime of martian waters based on the dissolution of rapidly dissolving phases (e.g., Elwood-Madden et al. 2009). Using the measured particle sizes, these estimates extend to 0.3-2.4 Myr. Lower temperatures, higher salinities (above ~0.05 M), and the presence of liquid water intermittently, rather than persistently, would additionally extend these lifetimes.

An important caveat to these lifetimes is that allophane does not generally form solid spherical particles; rather, it forms loose aggregates that span tens of microns, each made up of hollow, porous nano-spheres ~5-50 nm in diameter (**Fig. 3** and **S6-S7**), which may not dissolve according to the shrinking sphere model. Although natural allophane is present in soils up to ~2 kyr old in tropical climates (Bleeker and Parfitt 1974) and in soils >30 kyr old in more temperate zones (Nagasawa 1978), allophane in these soils may exist as an intermediate material, being simultaneously formed and transformed to more ordered phases or dissolved, potentially in different zones of the soil. Regions where allophane is present would then represent an environment where the accumulation rate of allophane is equal to or greater than the rate at which allophane is transformed or dissolved, and not necessarily regions where allophane particle lifetimes are tens of thousands of years.

Characterization of reacted materials

XRD Samples of Fe-free allophane, Fe-poor allophane, and Fe-rich allophane from each experiment were examined with XRD to investigate possible formation of secondary phases. No well-crystalline products, such as gibbsite or hematite, were present above the detection limit of the instrument (~1 wt. %); however, a broad, low-angle peak developed as a result of alteration in Fe-free allophane reacted at pH_0 3, 7, and 10; in Fe-poor allophane reacted at pH_0 3; and in Fe-rich allophane reacted at pH_0 10 (**Fig. 8** and **S15**). This broad peak occurs near 11-12 Å, larger than the typical (001) d-spacing for kaolinite (~7.2 Å, Goodyear and Duffin 1961) and smaller than that of type examples of hydrated smectites (13.5-15 Å, Moore and Reynolds 1997), although similar to the (001) peak observed by Pickering (2014) in the partially hydrated SWy-2 Na-montmorillonite (11.8 Å) and certain other samples of montmorillonite (e.g., Kloprogge et al. 2002, with d-spacings of 11.5-15.0 Å). The 11-12 Å peak could alternately be due to the collapse of a smectite-like phase due to exposure to vacuum during freeze-drying (e.g., Frushour and Bish, 2017). Therefore, this broad peak may represent the early development of a clay mineral, as also seen in the HRTEM results. The observed peak positions for all reacted and unreacted materials are given in **Table 8**.

Microscopy Analyses by SEM of pH_0_3_FRA (pH_{steady} ~4) reacted for two days and for one month revealed that the grain texture tended to become more porous with increasing dissolution time, and that the grains themselves tended to become smaller (**Fig. S16-S17**), possibly indicating the presence of less ordered material that dissolves more rapidly than the surrounding material, causing disaggregation. Analyses of reacted materials by SEM are summarized in **Table S1**.

After a 2-month reaction time, pH_0_10_FRA showed the formation of small (~2 μm) linear features within the larger Fe-rich allophane aggregates (**Fig. 9a** and **S18**) in HRTEM analysis (analyses of reacted materials by HRTEM are summarized in **Table S7**). These features were interpreted as the rolled or curled edges of silicate sheets, possibly due to the incipient conversion to phyllosilicate. Similar features have been observed in synthetic hisingerite-like Si-Fe precipitates, and were also interpreted as the edges of phyllosilicate sheets (Decarreau et al. 1987). Overall, the material was still poorly crystalline, and the linear features did not demonstrate a higher degree of crystallinity than the surrounding masses, as demonstrated by their lack of lattice fringes. The linear features were also observed in pH_0_3_FRA reacted for 6 months, although they were much less prevalent (**Fig. S19**). In contrast, no linear features were observed in unaltered Fe-rich allophane.

Only a few of these linear "edge-curl" features were observed in pH_0_10_FFA reacted for 2 months (**Fig. S20**). Fe-free allophane also maintained the morphological dichotomy between a "rugged" texture and a "blobby" texture (**Fig. 9b**) seen in the unreacted material. The "blobby" texture was rapidly destroyed by the high-energy STEM beam, while the "rugged" texture was more robust, suggesting a higher degree of hydration in the "blobby" material (**Fig. S21**; Decarreau et al. 1987). This extreme beam-sensitivity was only directly observed in the altered Fe-free allophane but may also be true of the unaltered Fe-free allophane. No "blobby" material was observed in the altered or unaltered Fe-rich allophane samples.

Total digestion Changes in bulk chemistry due to dissolution are given in **Table 6**. Total digestions show that SiO_2 was preferentially released from some samples (e.g., pH_0_7_FPA), while others (e.g., pH_0_7_FFA) maintained relatively stable SiO_2 content. The amount of SiO_2 released during dissolution of Fe-rich allophane correlated well with the change in bulk SiO_2 content measured by total digestion (**Fig. S22**). Neither Fe-poor allophane nor Fe-rich allophane showed detectable differences in Fe_2O_3 between experimental conditions and the unreacted samples. The observed enrichment in Al_2O_3 in some samples (e.g., pH_0_10_FFA) is due to a net loss of SiO_2 from the samples. This is corroborated by the pH_0_7_FPA experiment, where the greatest net loss of SiO_2 (~1 wt.% versus the unreacted sample) is accompanied by the greatest enrichment in Al_2O_3 (~12 wt.% versus the unreacted sample). No correlation between SiO_2 loss and Al_2O_3 enrichment or loss was observed in the Fe-rich allophane samples.

DISCUSSION

Comparison of synthetic and martian amorphous materials

Comparison of synthetic materials to phases found on the martian surface is necessary to ensure that they are appropriate functional analogs. These synthetic analogs can help elucidate properties of the amorphous component in martian rocks and soils that cannot be examined with current remote instrumentation, such as dissolution kinetics, micro-morphology, and formation of secondary phases.

The XRD patterns of synthesized Fe-free allophane, Fe-poor allophane, and Fe-rich allophane all have broad peaks centered around 28º 2θ Co Kα (3.39-3.5 Å, **Fig. 2b**, **Tables 5** and **8**), similar to the amorphous humps in the CheMin patterns of samples from Gale crater (**Fig. 10**), including the Rocknest “soil” sample and the Cumberland, John Klein, and Windjana rock samples (Bish et al. 2013; Achilles et al. 2017). Mass-balance calculations (e.g., Dehouck et al. 2014; Vaniman et al. 2014; Achilles et al. 2017; Morrison et al. 2018; Rampe et al. 2018) provided a range of possible compositions for the martian amorphous component, bearing in mind that the compositions may be slightly skewed by the presence of crystalline phases in abundances below the CheMin detection limit (e.g., Smith et al. 2018; Rampe et al. 2020; **Table S6**). The Al contents of the synthesized Fe-free allophane, Fe-poor allophane, and Fe-rich allophane are much higher than that of the martian amorphous component (**Table S6**), which may be due to the presence of other high-silica and high-Fe phases, such as high-silica glasses (e.g., 72.5 wt.% SiO_2, 9.36 wt.% Al_2O_3, 0.95 wt.% FeO; Beard et al. 2015) and/or opaline silica, Fe-oxides, and Fe-sulfates in the martian samples (Achilles et al. 2017; Rampe et al. 2017). Alternately, Al-rich amorphous materials, such as allophane, may simply not be present in the Mars amorphous material. The high Fe and Si contents of the martian material indicate that hisingerite (~33.5 wt.% Fe, ~16.8 wt.% Si; Henmi et al. 1980) or a co-occurrence of ferrihydrite and amorphous silica are plausible component phases (Dehouck et al. 2017).

The EGA data of the synthetic samples used in this study (**Fig. S3-S4**) were dominated by water release at ~130-400ºC. SAM data from the Rocknest, Cumberland, John Klein, and Windjana samples in Gale crater showed H_2O release primarily between 100-450ºC, likely including releases from hydrated sulfates and clay minerals (Leshin et al. 2013; Sutter et al. 2017). Sutter et al. (2017) predict adsorbed water release, perhaps due to allophane and other amorphous phases, below ~200ºC, and Leshin et al. (2013) attribute water release from martian samples at ~110ºC to allophane. These values (≤200ºC and ~110ºC) are consistent with the measured release at ~130-400ºC from the samples examined in this study. Therefore, although only a small fraction of the water release from samples at Gale crater is attributed to amorphous materials, measurements of these synthetic allophanes agree well with that fraction.

Based on current data and the results of XRD, total chemistry, and EGA analyses, therefore, synthetic Fe-free allophane, Fe-poor allophane, and Fe-rich allophane are appropriate analogs for at least portions of the amorphous component in modern martian soils and ancient sedimentary rocks and can be used to help better understand these amorphous materials.

Dissolution rates and rate laws

The dissolution rates measured for Fe-free allophane, Fe-poor allophane, and Fe-rich allophane are within 10% of each other (**Fig. 7**) and are approximately an order of magnitude faster than dissolution rates of crystalline clay minerals of similar compositions, such as nontronite (Gainey et al. 2014; Steiner et al. 2016) and montmorillonite (e.g., Huertas et al. 2001; Rozalen et al. 2008) (**Fig. 11**). This trend is consistent with trends observed for other amorphous or poorly crystalline materials; amorphous Al and Fe phosphates dissolve more rapidly than crystalline Al and Fe phosphates (Huffman 1960; Tu et al. 2014), and amorphous silica dissolves more rapidly than quartz (Liang and Readey 1987). However, the surface area-normalized dissolution rates measured for Fe-free allophane, Fe-poor allophane, and Fe-rich allophane are similar to those measured for goethite at pH ~3 (Cheah et al. 2003), amorphous silica at pH ~3 (Icenhower and Dove 2000), and alunite at pH ~3-5 (Miller et al. 2016) at the same pH values, and are slower than the surface area-normalized dissolution rates measured for basaltic glass (Gislason and Oelkers 2003) and jarosite (Elwood-Madden et al. 2012) across the pH range (**Fig. 11a**). Based on the surface area-normalized dissolution rates, interactions between liquid water and poorly crystalline silicate phases, such as allophane and hisingerite, release cations and silica into solution more rapidly than well-crystalline silicate phases with similar compositions (especially when there is polymerized Si in the interior of the allophane or hisingerite nano-spherules), but at rates similar to or slightly slower than well-crystalline Fe/Al-sulfates and Fe-oxides and amorphous silica. However, the samples used in this study have very high BET surface areas (380-510 m^2 g^{-1}, **Table 1**) and BET surface area is not a perfect proxy for reactive surface area (e.g., Gautier et al. 2001). For example, in both martian and terrestrial environments, mineral dissolution is likely affected by the surface area accessible to water, which may be affected by the size of allophane aggregates (Karube et al. 1996) or armoring of allophane surfaces by secondary precipitates. To account for the very high specific surface areas of these materials, the measured dissolution rates were also normalized to the mass of material in the reactor (**Fig. 11b**). The mass-normalized dissolution rates of these synthetic materials are faster than those of montmorillonite, nontronite, goethite, and basaltic glass, and are similar to those of amorphous silica, alunite, and jarosite.

A low pH dependence is observed for dissolution of all materials in the initial pH range from 3 to 10 (Fe-free allophane, n = 0.145 ± 0.028, Fe-poor allophane, n = 0.222 ± 0.040, and Fe-rich allophane, n = 0.042 ± 0.016). These dependences are much lower than for other silicates with similar compositions; for example, for montmorillonite, n = 0.34, and nontronite, n = 0.297, under acidic conditions (Huertas et al. 2001; Gainey et al. 2014). Based on dissolution experiments with naturally occurring allophane conducted by Abidin et al. (2004), the pH dependence of allophane dissolution likely increases dramatically above pH ~10, similar to the trend observed in the pH dependence of kaolinite dissolution (n_{OH-} = 0.472, Palandri and Kharaka 2004 and references therein). In both materials, this is likely due to the increased solubility of silica and aluminum at high pH.

The dissolution behavior of Fe-free allophane, Fe-poor allophane, and Fe-rich allophane—similar dissolution rates, with low reaction orders with respect to pH—may be explained by the structures of allophane and hisingerite. Allophane consists of hollow, porous nano-spherules ~5 nm (50 Å) in diameter, formed from a rolled silica sheet surrounded by a gibbsite sheet (Iyoda et al. 2012; Wada 1989). Additional polymerized Si is contained in the interior of the nano-spherules when the Al:Si ratio is less than ~2:1 (Jeute et al. in press; Childs et al. 1990; Parfitt 1990). Although gibbsite dissolution has a large reaction order with respect to pH (n = 0.992) (Palandri and Kharaka 2004), dissolution of pure silica phases, such as amorphous silica, does not depend on pH (e.g., Palandri and Kharaka 2004). Therefore, dissolution rates based on Si release rates would be expected to be relatively insensitive to pH because the interior polymerized Si can enter solution through the nano-spherule pores regardless of the rate at which the gibbsite layer is dissolved. In the high-acidity experiments

(pH_0 3), an initial preferential leaching of Al is observed, consistent with the rapid dissolution of an Al-rich layer, and little variation in dissolution rate based on silica release rate is observed across the range of pH conditions, consistent with the mostly independent dissolution of interior silica.

A similar layered nano-spherule structure is observed in hisingerite (Shayan 1984; Eggleton and Tilley 1998) and may also exist in Fe-rich allophane. However, the hisingerite layers occur in multiple concentric sheets, similar to the structure of true phyllosilicates, and form nano-spherules up to 200 Å in diameter (Shayan 1984). These multiple concentric layers may reduce the dissolution rate under acidic conditions by protecting the interior of the spherules from protons in solution. Precipitation of Fe-oxide phases on the surface of hisingerite particles might also inhibit further dissolution by blocking pores or access to surface sites. The dissolution reactions of these synthetic allophanes (e.g. *Eq. (5)*, Section S8) also help explain the lower pH dependence of Fe-rich allophane than the Fe-free and Fe-poor allophanes by demonstrating the reduced consumption/production of H^+ by Fe-rich allophane versus Fe-free allophane and Fe-poor allophane.

Release of Fe and Al from synthetic materials in this study was approximately equal to or below stoichiometric values with respect to Si (**Fig. 6**), with all Fe:Si and Al:Si ratios below stoichiometric values when pH_{steady} was reached. This non-stoichiometric dissolution indicates that the altered material is likely more Al- and Fe-rich than the starting material, as supported by chemical composition of the reacted samples (**Table 8**). Aluminum (and Fe if present) is first leached rapidly from the gibbsite sheet in the nano-spherules (**Data Sheets S29-S38**), and then may be reprecipitated or adsorbed, as indicated by the decrease of solution concentrations of Al and Fe with time.

Secondary phases and altered material

Allophane and hisingerite are generally considered to occur as intermediates in the formation of more stable phases, such as kaolinite and nontronite (Wada 1989). Generally, during the weathering process, silica and aluminum or iron can combine to form allophane and/or hisingerite, which are then converted to imogolite or halloysite, and then to more mature layer silicates (Wada 1989). However, despite the studies examining these large-scale transitions, little work has examined the incipient weathering of poorly crystalline phases such as allophane and hisingerite (e.g., Farmer et al. 1991; Farmer 1997). This study shows that under alkaline conditions, layered, phyllosilicate-like precursor materials form rapidly (on the order of a few months) from Fe-free and Fe-rich allophane under laboratory conditions, in agreement with previous work by Farmer et al. (1991) and Farmer (1997), which examined weathering of hisingerite under high temperatures and in calcareous conditions at both high and low temperatures.

FE-STEM analyses of pH_0_10_FRA reacted for 2 months (pH_{steady} ~8) showed linear "edge-curl" features that were not present in the unreacted materials (**Fig. 4a**, **4c**, **9a**, and **S18**). At low pH, fewer of these linear features were observed (**Fig. S19**). This observation supports the XRD data that indicate incipient phyllosilicate formation from Fe-rich allophane is less favorable at low pH than at alkaline pH.

As described above, Fe-free allophane and Fe-poor allophane show fewer phyllosilicate-like "edge-curl" features than Fe-rich allophane when reacted under alkaline pH conditions for 2 months (**Fig. S20-S21**). The Fe-rich allophane may behave differently than the Fe-poor and Fe-free allophanes because of reprecipitation or reduced dissolution of the Fe-containing material, as evidenced by the decrease in Fe concentration in solution with time (see **Fig. 1**, **Fig. 6**, and **Fig. S9**). Reprecipitated Fe-containing material, in combination with the silica-rich solution generated during alteration at alkaline pH, may create a favorable environment for incipient phyllosilicate characteristics to develop, similar to the formation of framework layers containing silica and divalent/trivalent cations during the synthesis of nontronite and saponite by the sol-gel method (e.g., Harder 1976; Harder 1978; Baldermann et al. 2014; Gainey et al. 2017) and the formation of some seafloor nontronites (Sun et al. 2011). Because the Fe-free and Fe-poor allophane lack significant Fe, they may be less likely to develop phyllosilicate precursor phases when exposed to alkaline Si-containing solutions.

Bulk chemistry of unreacted and reacted samples (**Table 6**) shows that some reacted samples underwent a net loss of Si versus the unreacted sample, while others did not. A net loss of Si was observed in Fe-rich allophane samples across the range of pH conditions studied here, although there was no clear correlation between net Si loss and the pH of the experiment. A net loss of Si was also observed in the pH_0_7_FPA experiment. No appreciable differences in Si content were observed between any of the Fe-free allophane samples. This observation indicates that the Si that dissolved from all of the Fe-free allophane experiments and all but one of the Fe-poor allophane experiments either a) reprecipitated before the end of the experiment (but was not detectable via XRD or microscopy), or b) did not dissolve in sufficient quantity to produce a detectable change in Si content of the final reacted material. Similarly, for the Fe-rich allophane experiments (and pH_0_7_FPA), Si may have dissolved in sufficient quantities to detectably affect the composition of the remaining solids, and not reprecipitated in sufficient quantities to erase the signature of its dissolution. The amount of Si released into solution during dissolution experiments and the amount of Si remaining in each sample was plotted to illustrate this relationship (**Fig. S22**).

Implications of experiments for Mars

The dissolution experiments with Fe-free and Fe-bearing allophane demonstrate rapid initial dissolution and enrichment of Al and Fe across the range of pH conditions. Silicon in the interiors of Fe-free allophane, Fe-poor allophane, and Fe-rich allophane nano-spherules is accessed through pores in the nano-spherule walls, dissolves rapidly with little dependence on pH, and tends to remain in solution. Aluminum and Fe from the nano-spherule walls may rapidly re-precipitate, readsorb, or not enter solution at all. FE-STEM analyses of reacted materials show diagnostic linear features (e.g., **Fig. 9a**) that are not seen in unreacted material, which are more prevalent at alkaline pH than at acidic pH. In the event that samples containing hisingerite or allophane are returned from Mars, similar features that indicate brief interaction with past liquid water (on the order of months to years) might be detectable. The rapid alteration of poorly crystalline silicate materials could be a useful tool for examining very short-lived episodes of water-rock interaction; on timescales where more crystalline silicate materials would show little to no chemical, mineralogical, or structural change due to interaction with water, poorly crystalline silicate materials may be significantly altered. However, evidence for limited water-rock interactions captured by poorly crystalline silicate materials in returned martian samples may not capture *in-situ* processes. Martian samples will be sealed in collection tubes and left on the surface for years before return to Earth. Hydrated materials may dehydrate diurnally or seasonally (e.g., Vaniman et al. 2018), potentially allowing water vapor to precipitate on particles in the sample tubes. The rapid dissolution rates of Fe-free allophane, Fe-poor allophane, and Fe-rich allophane suggest that these materials may be altered if sufficient water is present during such a scenario and, therefore, samples should be returned rapidly to limit alteration within sample tubes.

The continued presence of allophanic materials in returned samples from Mars could indicate that interactions of liquid water with the amorphous component were limited, consistent with other observations of mineral assemblages in Gale crater (e.g., the co-occurrence of jarosite and fluorapatite, as discussed by Rampe et al. 2017). Although the dissolution rates of all three synthetic materials were fastest at pH_0 3, and slower at more alkaline pH conditions, the range between the fastest and slowest dissolution rates spans less than an order of magnitude. Therefore, allophane or hisingerite on Mars would have dissolved or altered to more crystalline phases rapidly if abundant liquid water was present, regardless of the water's pH, although field dissolution rates are expected to be ~2 orders of magnitude slower than the dissolution rates measured in laboratory experiments (e.g., Velbel 1993; Zhu et al. 2016). The temperatures on Mars when liquid water was present were also likely much lower than 25°C, which would further slow dissolution and extend the lifetimes of allophane or hisingerite. However, waters with low salt concentrations, such as those that might be found in the "dilute lake waters" that may have filled Gale crater (Rampe et al. 2017), can significantly enhance dissolution of Si-rich phases like quartz and amorphous silica (e.g., Dove and Nix 1997; Icenhower and Dove 2000). Higher concentrations of salts tend to slow dissolution rates across a range of minerals, with dissolution rates slowing in proportion to decreasing water activity (Pritchett et al. 2012; Olsen et al. 2015; Steiner et al. 2016), and high ionic strength brines, such as those proposed by Tosca et al. (2008) as the global norm throughout most of martian history, could result in significantly reduced dissolution rates and even further extend the lifetimes of rapidly dissolving phases.

Amorphous materials have been found in all samples examined to date in Gale crater, with the relative proportion of amorphous material increasing from ~20 wt.% at the base of Mt. Sharp to >50 wt.% in formations farther up section (e.g., Frydenvang et al. 2017; Rampe et al. 2017; Yen et al. 2017). The amorphous material in the Pahrump Hills member becomes increasingly silicic as the amount present in samples increases, although this may be due to a more silicic source rock (Morris et al. 2016; Rampe et al. 2017). Likewise, the amount of smectite decreases along the traverse up-section into Pahrump Hills until smectite abundance falls below CheMin's detection limit, while phases produced by acidic alteration (e.g., jarosite) are sandwiched between the silica-rich and smectite-rich members (Morrison et al. 2018). Little olivine is observed in the rock samples from Gale crater, but olivine is present in higher proportion in the aeolian samples, which are considered to be representative of the bulk Mars crust (e.g., Bish et al. 2013; Blake et al. 2013; Meslin et al. 2013; Morrison et al. 2018). Taken together, these lines of evidence indicate that the rocks in Gale crater have undergone significant *in-situ* chemical alteration (e.g., Yen et al. 2017; Hausrath et al. 2018; Morrison et al. 2018), although the presence of a non-equilibrium mineral assemblage, including jarosite, fluorapatite, and perhaps allophane or hisingerite, indicates that aqueous alteration was either time-limited or occurred in multiple stages, with the later stages being both briefer and more acidic than those that preceded them (e.g., Rampe et al. 2017; Yen et al. 2017; Hausrath et al. 2018).

Based on the proposed chemical composition of the amorphous material and the presence of Fe-rich clay minerals in the stratigraphically lowest mudstones of Gale crater (Cumberland and John Klein), the amorphous material observed in these samples may contain a significant hisingerite component (Dehouck et al. 2017). This hisingerite could represent an intermediate between primary olivine/pyroxene and the smectite clay minerals. These mudstones are the most likely of the samples from Gale crater that have been examined so far to contain hisingerite due to their Fe- and Si-rich compositions, high proportions of clay minerals, and limited interaction with acidic waters (Bish et al. 2017). At the top of the Pahrump Hills member, where the amorphous component is predominantly amorphous silica, there are no detectable smectites, indicating that either a) both the smectites and their precursor phases (i.e., hisingerite) have been dissolved, or b) that no smectites or precursor phases ever formed there. The presence of acid alteration products and multiple cation deficiencies in these locations point to extensive leaching by acidic groundwater. Acidic ground waters would be expected to rapidly dissolve any hisingerite that was present in these rocks, producing abundant amorphous silica as a leachate, and the subsequent dissolution of this silica may have been less rapid. However, a more silicic sediment source may be responsible for the observed silica enrichment in Pahrump Hills (Morris et al. 2016; Rampe et al. 2017), with acid alteration playing a more minor role, possibly during late-stage diagenesis.

CONCLUSIONS

Dissolution experiments with synthetic Fe-free allophane, Fe-poor allophane, and Fe-rich allophane in the range of initial pH_0 3-10 indicate rapid initial dissolution, approximately an order of magnitude faster than that of well-crystalline clay minerals of similar composition. The dissolution rates based on Si release of all three materials showed little pH dependence across the experimental pH range. For Fe-free allophane, $\log r_{diss} = -10.65 - 0.15 \times \text{pH}$; for Fe-poor allophane, $\log r_{diss} = -10.35 - 0.22 \times \text{pH}$; and for Fe-rich allophane, $\log r_{diss} = -11.46 - 0.042 \times \text{pH}$ at 25°C, where r_{diss} has the units of mol m^{-2} s^{-1}. Experimental results indicate that poorly crystalline allophane-like materials in Gale crater would have dissolved rapidly when exposed to liquid water regardless of the water's pH. The detection of poorly crystalline materials in Gale crater suggests that interaction of liquid water with these materials was limited after the X-ray amorphous materials formed. In the case of more prolonged interactions, the materials would be expected to have either dissolved completely, or altered to form more stable phases. Dissolution in Gale crater would likely have proceeded significantly more slowly than in these experiments, with particle lifetimes on the order of tens of thousands to hundreds of thousands of years, due to the lower temperature and higher salinity expected for Mars' ancient waters as well as generally slower dissolution rates in the field than in the laboratory.

Analyses with FE-STEM of reacted Fe-free and Fe-rich allophane revealed structural changes, including the formation of layered phyllosilicate-like structures within poorly crystalline agglomerates, after only a few months of reaction time. Such structural changes may be a useful tool for interpreting the weathering history of returned martian samples that have had limited interactions with liquid water.

Examination of Fe-free allophane, Fe-poor allophane, and Fe-rich allophane may be critical to understanding the characteristics of short-lived martian waters. These phases may provide insight into the duration of short-lived liquid water in Gale crater by allowing examination of aqueous alteration features at a finer timescale than that provided by well-crystalline, aqueously altered minerals. With continued investigation and characterization, the properties of the Mars amorphous component could be used to constrain and elucidate the characteristics of Mars' most recent waters.

ACKNOWLEDGMENTS

We would like to acknowledge the following people for their contributions to this research: Brad Sutter, Lisa Danielson, Joanna Hogancamp, Toluwalope Bamisile, Chris Adcock, Seth Gainey, Peter Sbraccia, Arlaine Sanchez, Ngoc Luu, Dave Hatchett, Minghua Ren, Michael Strange, and Richard Panduro-Allanson. We also thank Editor-in-Chief Professor Joseph W. Stucki, the associate editors of *Clays and Clay Minerals,* and our reviewers for their insightful comments on this manuscript. This work was supported by the NASA Mars Data Analysis Program (grant #80NSSC17K0581), the University of Nevada, Las Vegas Faculty Opportunity Award, the University of Nevada, Las Vegas Doctoral Award, the Geological Society of America Graduate Research Grant, the University of Nevada, Las Vegas Graduate and Professional Student Association research and travel grants, and the Southwest Travel Award.

DECLARATIONS

Funding

This work was supported by the NASA Mars Data Analysis Program (grant #80NSSC17K0581), the University of Nevada, Las Vegas Faculty Opportunity Award, the University of Nevada, Las Vegas Doctoral Award, the Geological Society of America Graduate Research Grant, the University of Nevada, Las Vegas Graduate and Professional Student Association research grant and travel grant, and the Southwest Travel Award.

Conflicts of interest/Competing interests

S. J. Ralston conducted this research while employed as a graduate student at the University of Nevada, Las Vegas and was employed by Jacobs prior to manuscript submission (multiple affiliation). Elisabeth Hausrath, Oliver Tschauner, Elizabeth Rampe, Tanya Peretyazhko, Roy Christoffersen, Christopher DeFelice, and Hyejeong Lee declare that they have no conflicts to report.

REFERENCES

Abidin, Z., Matsue, N., & Henmi T. (2004) Dissolution mechanism of nano-ball allophane with dilute alkali solution. *Clay Science* **12**, 213-222.

Achilles, C.N., Downs, R.T., Ming, D.W., Rampe, E.B., Morris, R.V., Treiman, A.H., Morrison, S.M., Blake, D.F., Vaniman, D.T., Ewing, R.C., Chipera, S.J., Yen, A.S., Bristow, T.F., Ehlmann, B.L., Gellert, R., Hazen, R.M., Fendrich, K.V., Craig, P.I., Grotzinger, J.P., Des Marais, D.J., Farmer, J.D., Sarrazin, P.C., & Morookian, J.M. (2017) Mineralogy of an active eolian sediment from the Namib dune, Gale crater, Mars. *Journal of Geophysical Research, Planets* **122**, 2344-2361.

Baker, L.L. & Strawn, D.G. (2014) Temperature effects on synthetic nontronite crystallinity and implications for nontronite formation in Columbia River Basalts, *Clays and Clay Minerals* **62**, 89-101.

Baker, L.L. & Strawn, D.G. (2012) Fe K-edge XAFS spectra of phyllosilicates of varying crystallinity. *Physics and Chemistry of Minerals* **39**, 675-684.

Baker, L.L., Nickerson, R.D., & Strawn, D.G. (2014) XAFS study of Fe-substituted allophane and imogolite, *Clays and Clay Minerals* **62**, 20-34.

Baldermann, A., Dohrmann, R., Kaufhold, S., Nickel, C., Letofsky-Papst, I., & Dietzel, M. (2014) The Fe-Mg-saponite solid solution series—a hydrothermal synthesis study. *Clay Minerals* **49**, 391-415.

Beard, A.D., Downes, H., & Chaussidon, M. (2015) Petrology of a nonindigenous microgranitic clast in polymict ureilite EET 87720: Evidence for formation of evolved melt on an unknown parent body. *Meteoritics & Planetary Science* **50**, 1613-1623.

Bibring, J.P., Langevin, Y., Mustard, J.F., Poulet, F., Arvidson, R., Gendrin, A., Gondet, B., Mangold, N., Pinet, P., Forget, F., Berthe, M., Bibring, J.P., Gendrin, A., Gomez, C., Gondet, B., Jouglet, D., Poulet, F., Soufflot, A., Vincendon, M., Combes, M., Drossart, P., Encrenaz, T., Fouchet, T., Merchiorri, R., Belluci, G., Altieri, F., Formisano, V., Capaccioni, F., Cerroni, P., Coradini, A., Fonti, S., Korablev, O., Kottsov, V., Ignatiev, N., Moroz, V., Titov, D., Zasova, L., Loiseau, D., Mangold, N., Pinet, P., Doute, S., Schmitt, B., Sotin, C., Hauber, E., Hoffmann, H., Jaumann, R., Keller, U., Arvidson, R., Mustard, J.F., Duxbury, T., Forget, F., & Neukum, G. (2006) Global mineralogical and aqueous mars history derived from OMEGA/Mars Express data. *Science* **312**, 400-404.

Bish, D.L. & Duffy, C.J. (1990) Thermogravimetric Analysis of Minerals. In *Thermal Analysis in Clay Science* (eds. J. W. Stucki and D. L. Bish). The Clay Minerals Society, pp. 95–189.

Bish, D.L., Blake, D.F., Vaniman, D.T., Chipera, S.J., Morris, R.V., Ming, D.W., Treiman, A.H., Sarrazin, P., Morrison, S.M., Downs, R.T., Achilles, C.N., Yen, A.S., Bristow, T.F., Crisp, J.A., Morookian, J.M., Farmer, J.D., Rampe, E.B., Stolper, E.M., Spanovich, N., & the MSL Science Team (2013) X-ray diffraction results from Mars Science Laboratory: mineralogy of Rocknest at Gale crater. *Science* **341**, 1238932.

Bishop, J.L. & Rampe E.B. (2016) Evidence for a changing Martian climate from the mineralogy at Mawrth Vallis. *Earth and Planetary Science Letters* **448**, 42-48.

Bishop, J.L., Rampe, E.B., Bish, D.L., Abidin, Z., Baker, L.L., Matsue, N., & Henmi T. (2013) Spectral and Hydration Properties of Allophane and Imogolite. *Clays and Clay Minerals* **61**, 57-74.

Blake, D.F., Morris, R.V., Kocurek, G., Morrison, S.M., Downs, R.T., Bish, D., Ming, D.W., Edgett, K.S., Rubin, D., Goetz, W., Madsen, M.B., Sullivan, R., Gellert, R., Campbell, I., Treiman, A.H., McLennan, S.M., Yen, A.S., Grotzinger, J., Vaniman, D.T., Chipera, S.J., Achilles, C.N., Rampe, E.B. Sumner, D., Meslin, P.Y., Maurice, S., Forni, O., Gasnault, O., Fisk, M., Schmidt, M., Mahaffy, P., Leshin, L.A., Glavin, D., Steele, A., Freissinet, C., Navarro-Gonzalez, R., Yingst, R.A., Kah, L.C., Bridges, N., Lewis, K.W., Bristow, T.F., Farmer, J.D., Crisp, J.A., Stolper, E.M., Marais, D.J.D., Sarrazin, P., & the MSL Science Team (2013) Curiosity at Gale crater, Mars: Characterization and Analysis of the Rocknest Sand Shadow. *Science* **341**, 1239505.

Bleeker, P. & Parfitt R.L. (1974) Volcanic ash and its clay mineralogy at Cape Hoskins, New Britain, Papua New Guinea. *Geoderma* **11**, 123-135.

Carr, M.H. (1996) Water erosion on Mars and its biologic implications. *Endeavour* **20**, 56-60.

Catalano, J.G. (2013) Thermodynamic and mass balance constraints on iron-bearing phyllosilicate formation and alteration pathways on early Mars. *Journal of Geophysical Research, Planets* **118**, 2124-2136.

Cheah, S.-F., Kraemer, S.M., Cervini-Silva, J., & Sposito G. (2003) Steady-state dissolution kinetics of goethite in the presence of desferrioxamine B and oxalate ligands: implications for the microbial acquisition of iron. *Chemical Geology* **198,** 63-75.

Childs, C.W., Parfitt, R.L. & Newman, R.H. (1990) Structural studies of Silica Springs allophane, *Clay Minerals* **25**, 329-341.

Decarreau, A., Bonnin, D., Badaut-Trauth, D., Couty, R., & Kaiser, P. (1987) Synthesis and crystallogenesis of ferric smectite by evolution of Si-Fe coprecipitates in oxidizing conditions. *Clay Minerals* **22,** 207-223.

DeFelice, C., Mallick, S., Saal, A.E., & Huang S. (2019) An isotopically depleted lower mantle component is intrinsic to the Hawaiian mantle plume. *Nature Geoscience* **12**, 487-492.

Dehouck, E., McLennan, S.M., Sklute, E.C., & Darby Dyar, M. (2017) Stability and fate of ferrihydrite during episodes of water/rock interactions on early Mars: An experimental approach. *Journal of Geophysical Research, Planets* **122,** 358-382.

Dehouck, E., McLennan, S.M., Meslin, P.Y., & Cousin, A. (2014) Constraints on abundance, composition, and nature of X-ray amorphous components of soils and rocks at Gale crater, Mars. *Journal of Geophysical Research, Planets* **119**, 2640-2657.

Denaix, L. (1993) Synthèse et propriétés d'aluminosilicates non lamellaires : l'imogolite et les allophanes, Sciences de la Terre. Université Pierre et Marie Curie (Paris 6), Paris, FRA, p. 223.

Dove, P.M. & Crerar, D.A. (1990) Kinetics of quartz dissolution in electrolyte solutions using a hydrothermal mixed flow reactor. *Geochimica et Cosmochimica Acta* **54,** 955-969.

Dove, P.M. & Nix C.J. (1997) The influence of the alkaline earth cations, magnesium, calcium, and barium on the dissolution kinetics of quartz. *Geochimica et Cosmochimica Acta* **61,** 3329-3340.

Eaton, A.D., Clesceri, L.S., Rice, E.W., Greenberg, A.E., & Franson M.A.H. (2005). Standard Methods for the Examination of Water and Wastewater. American Public Health Association, Washington, DC. Eggleton R.A. (1977) Nontronite: chemistry and X-ray diffraction. *Clay Minerals* **12**, 181-194.

Eggleton, R.A. & Tilley, D.B. (1998) Hisingerite: a ferric kaolin mineral with curved morphology. *Clays and Clay Minerals* **46**, 400-413.

Elwood-Madden, M.E., Madden, A.S., Rimstidt, J.D., Zahrai, S., Kendall, M.R., & Miller M.A. (2012) Jarosite dissolution rates and nanoscale mineralogy. *Geochimica et Cosmochimica Acta* **91,** 306-321.

Elwood-Madden, M.E., Madden, A.S., & Rimstidt J.D. (2009) How long was Meridiani Planum wet? Applying a jarosite stopwatch to determine the duration of aqueous diagenesis. *Geology* **37,** 635-638.

Farmer, V. (1997) Conversion of ferruginous allophanes to ferruginous beidellites at 95° under alkaline conditions with alternating oxidation and reduction, *Clays and Clay Minerals* **45**, 591-597.

Farmer, V., Krishnamurti, G., & Huang, P. (1991) Synthetic allophane and layer-silicate formation in SiO2-Al2O3-FeO-Fe2O3-MgO-H2O systems at 23 C and 89 C in a calcareous environment, *Clays and Clay Minerals* **39**, 561-570.

Frink, C.R. & Peech, M. (1963) Hydrolysis of the aluminum ion in dilute aqueous solutions. *Inorganic Chemistry* **2,** 473-478.

Frushour, A.M. & Bish, D.L. (2017). Laboratory studies of smectite chloritization: applications to the clay mineralogy of Gale crater, Mars. *Lunar Planet. Sci. XLVIII.* Lunar Planet. Inst., Houston, #2622(abstr.).

Frydenvang, J., Gasada, P.J., Hurowitz, J.A., Grotzinger, J.P., Wiens, R.C., Newsom, H.E., Edgett, K.S., Watkins, J., Bridges, J.C., Maurice, S., Risk, M.R., Johnson, J.R., Rapin, W., Stein, N.T., Clegg, S.M., Schwenzer, S.P., Bedford, C.C., Edwards, P., Mangold, N., Cousin, A., Anderson, R.B., Payré, V., Vaniman, D., Blake, D.F., Lanza, N.L., Gupta, S., Van Beek, J., Sautter, V., Meslin, P.Y., Rice, M., Milliken, R., Gellert, R., Thompson, L., Clark, B.C., Sumner, D.Y., Fraeman, A.A., Kinch, K.M., Madsen, M.B., Mitrofanov, I.G., Jun, I., Calef, F., & Vasavada A.R. (2017) Diagenetic silica enrichment and late-stage groundwater activity in Gale crater, Mars. *Geophysical Research Letters* **44**, 4716-4724.

Gainey, S.R., Hausrath, E.M., Adcock, C.T., Tschauner, O., Hurowitz, J.A., Ehlmann, B.L., Xiao, Y., & Bartlett, C.L. (2017) Clay mineral formation under oxidized conditions and implications for paleoenvironments and organic preservation on Mars. *Nature Communications* **8**, 1230.

Gainey, S.R., Hausrath, E.M., Hurowitz, J.A., & Milliken, R.E. (2014) Nontronite dissolution rates and implications for Mars. *Geochimica et Cosmochimica Acta* **126**, 192-211.

Gautier, J.-M., Oelkers, E.H., & Schott, J. (2001) Are quartz dissolution rates proportional to B.E.T. surface areas? *Geochimica et Cosmochimica Acta* **65,** 1059-1070.

Gibbons, R.D., Grams, N.E., Jarke, F.H., & Stoub, K.P. (1991) Practical quantitation limits. *Chemometrics and Intelligent Laboratory Systems* **12**, 225-235.

Gislason, S.R. & Oelkers, E.H. (2003) Mechanism, rates, and consequences of basaltic glass dissolution: II. An experimental study of the dissolution rates of basaltic glass as a function of pH and temperature. *Geochimica et Cosmochimica Acta* **67,** 3817-3832.

Goodyear, J. & Duffin, W.J. (1961) An X-ray examination of an exceptionally well crystallized kaolinite. *Mineralogical Magazine* **32**, 902-907.

Grotzinger, J.P., Gupta, S., Malin, M.C., Rubin, D.M., Schieber, J., Siebach, K., Sumner, D.Y., Stack, K.M., Vasavada, A.R., Arvidson, R.E., Calef 3rd, F., Edgar, L., Fischer, W.F., Grant, J.A., Griffes, J., Kah, L.C., Lamb, M.P., Lewis, K.W., Mangold, N., Minitti, M.E., Palucis, M., Rice, M., Williams, R.M., Yingst, R.A., Blake, D., Blaney, D., Conrad, P., Crisp, J., Dietrich, W.E., Dromart, G., Edgett, K.S., Ewing, R.C., Gellert, R., Hurowitz, J.A., Kocurek, G., Mahaffy, P., McBride, M.J., McLennan, S.M., Mischna, M., Ming, D., Milliken, R., Newsom, H., Oehler, D., Parker, T.J., Vaniman, D., Wiens, R.C., & Wilson, S.A. (2015) Deposition, exhumation, and paleoclimate of an ancient lake deposit, Gale crater, Mars. *Science* **350**, aac7575.

Gustafsson, J.P., Karltun, E., & Bhattacharya P. (1998) Allophane and imogolite in Swedish soils. Royal Institute of Technology (KTH), Stockholm.

Harder, H. (1978) Synthesis of iron layer silicate minerals under natural conditions. *Clays and Clay Minerals* **26**, 65-72.

Harder, H. (1976) Nontronite synthesis at low temperatures. *Chemical Geolology* **18**, 169-180.

Hausrath, E.M., Ming, D.W., Peretyazhko, T.S., & Rampe, E.B. (2018) Reactive transport and mass balance modeling of the Stimson sedimentary formation and altered fracture zones constrain diagenetic conditions at Gale crater, Mars. *Earth and Planetary Science Letters* **491,** 1-10.

Helm, L. & Merbach, A.E. (2005) Inorganic and Bioinorganic Solvent Exchange Mechanisms. *Chemical Reviews* **105,** 1923-1959.

Henmi, T., Wells, N., Childs, C.W., & Parfitt R.L. (1980) Poorly-ordered iron-rich precipitates from springs and streams on andesitic volcanoes. *Geochimica et Cosmochimica Acta* **44**, 365-372.

Hisinger, W. (1828) Analyse des mit dem Namen Hisingerit belegten Eisensilicats. *Annalen der Physik und Chemie* von J.C. Poggendorff Bd **13**, 13-508.

Hsu, P.H. (1976) Comparison of iron(III) and aluminum in precipitation of phosphate from solution. *Water Research* **10,** 903-907.

Huertas, F.J., Caballero, E., Jiménez de Cisneros, C., Huertas, F., & Linares J. (2001). Kinetics of montmorillonite dissolution in granitic solutions. *Applied Geochemistry* **16,** 397-407.

Huffman, E.O. (1960) Rates and mechanisms of dissolution of some ferric phosphates. *Soil Science,* 1-8.

Icenhower, J.P. & Dove P.M. (2000) The dissolution kinetics of amorphous silica into sodium chloride solutions: Effects of temperature and ionic strength. *Geochimica et Cosmochimica Acta* **64,** 4193-4203.

Ingles, O.G. & Willoughby, D.R. (1967) An Occurrence of Hisingerite with Evidence of Its Genesis. *Soil Science* **104**, 383-385.

Iyoda, F., Hayashi, S., Arakawa, S., John, B., Okamoto, M., Hayashi, H., & Yuan, G.D. (2012) Synthesis and adsorption characteristics of hollow spherical allophane nano-particles. *Applied Clay Science* **56**, 77-83.

Jeute, T., Baker, L.L., Bishop, J.L., Abidin, Z., & Rampe, E.B. (2021) Spectroscopic analysis of allophane and imogolite samples with variable Fe abundance for characterizing the poorly crystalline components on Mars. *American Mineralogist,* in press.

Karube, J., Nakaishi, K., Sugimoto, H., & Fujihira, M. (1996) Size and shape of allophane particles in dispersed aqueous systems, *Clays and Clay Minerals* **44**, 485-491.

Kitagawa, Y. (1973) Substitution of aluminum in allophane by iron. *Clay Science* **4,** l5l-154.

Kloprogge, J.T., Evans, R., Hickey, L., & Frost, R.L. (2002) Characterization and Al-pillaring of smectites from Miles, Queensland (Australia). *Applied Clay Science* **20,** 157-163.

Lamb, A.B. & Jacques, A.G. (1938) The slow hydrolysis of ferric chloride in dilute solutions-II. The change in hydrogen ion concentration. *Journal of the American Chemical Society* **60,** 1215-1225.

Lasaga, A.C. (1984) Chemical kinetics of water-rock interactions. *Journal of Geophysical Research* **89,** 4009-4025.

Leshin, L.A., Mahaffy, P.R., Webster, C.R., Cabane, M., Coll, P., Conrad, P.G., Archer Jr., P.D., Atreya, S.K., Brunner, A.E., Buch, A., Eigenbrode, J.L., Flesch, G.J., Franz, H.B., Freissinet, C., Glavin, D.P., McAdam, A.C., Miller, K.E., Ming, D.W., Morris, R.V., Navarro-Gonzalez, R., Niles, P.B., Owen, T., Pepin, R.O., Squyres, S., Steele, A., Stern, J.C., Summons, R.E., Sumner, D.Y., Sutter, B., Szopa, C., Teinturier, S., Trainer, M.G., Wray, J.J., Grotzinger, J.P., & the MSL Science Team (2013) Volatile, isotope, and organic analysis of martian fines with the Mars Curiosity rover. *Science* **341**, 1238937.

Liang, D.-T. & Readey, D.W. (1987) Dissolution Kinetics of Crystalline and Amorphous Silica in Hydrofluoric-Hydrochloric Acid Mixtures. *Journal of the American Ceramic Society* **70**, 570-577.

Meslin, P.Y., Gasnault, O., Forni, O., Schroder, S., Cousin, A., Berger, G., Clegg, S.M., Lasue, J., Maurice, S., Sautter, V., Le Mouelic, S., Wiens, R.C., Fabre, C., Goetz, W., Bish, D., Mangold, N., Ehlmann, B., Lanza, N., Harri, A.M., Anderson, R., Rampe, E., McConnochie, T.H., Pinet, P., Blaney, D., Leveille, R., Archer, D., Barraclough, B., Bender, S., Blake, D., Blank, J.G., Bridges, N., Clark, B.C., DeFlores, L., Delapp, D., Dromart, G., Dyar, M.D., Fisk, M., Gondet, B., Grotzinger, J., Herkenhoff, K., Johnson, J., Lacour, J.L., Langevin, Y., Leshin, L., Lewin, E., Madsen, M.B., Melikechi, N., Mezzacappa, A., Mischna, M.A., Moores, J.E., Newsom, H., Ollila, A., Perez, R., Renno, N., Sirven, J.B., Tokar, R., de la Torre, M., d'Uston, L., Vaniman, D., Yingst, A., & the MSL Science Team (2013) Soil Diversity and Hydration as Observed by ChemCam at Gale crater, Mars. *Science* **341**.

Miller, J.L., Elwood-Madden, A.S., Phillips-Lander, C.M., Pritchett, B.N., & Elwood-Madden M.E. (2016). Alunite dissolution rates: Dissolution mechanisms and implications for Mars. *Geochimica et Cosmochimica Acta* **172,** 93-106.

Milliken, R.E. & Bish D.L. (2014) Distinguishing hisingerite from other clays and its importance for Mars. *Lunar Planet. Sci. XLV.* Lunar Planet. Inst., Houston, #2251(abstr.).

Milliken, R.E., Swayze, G.A., Arvidson, R.E., Bishop, J.L., Clark, R.N., Ehlmann, B.L., Green, R.O., Grotzinger, J.P., Morris, R.V., Murchie, S.L., Mustard, J.F., & Weitz C. (2008) Opaline silica in young deposits on Mars. *Geology* **36**, 847.

Montarges-Pelletier, E., Bogenez, S., Pelletier, M., Razafitianamaharavo, A., Ghanbaja, J., Lartiges, B., and Michot L. (2005) Synthetic allophane-like particles: textural properties. *Colloids and Colloid Surfaces A: Physicochemical and Engineering Aspects* **255**, 1-10.

Morris, R.V., Vaniman, D.T., Blake, D.F., Gellert, R., Chipera, S.J., Rampe, E.B., Ming, D.W., Morrison, S.M., Downs, R.T., Treiman, A.H., Yen, A.S., Grotzinger, J.P., Achilles, C.N., Bristow, T.F., Crisp, J.A., Des Marais, D.J., Farmer, J.D., Fendrich, K.V., Frydenvang, J., Graff, T.G., Morookian, J.M., Stolper, E.M., & Schwenzer, S.P. (2016) Silicic volcanism on Mars evidenced by tridymite in high-SiO2 sedimentary rock at Gale crater. *Proceedings of the National Academy of Sciences of the United States of America* **113**, 7071-7076.

Morris, R.V., Golden, D.C., Bell, J.F., Shelfer, T.D., Scheinost, A.C., Hinman, N.W., Furniss, G., Mertzman, S.A., Bishop, J.L., Ming, D.W., Allen, C.C., & Britt, D.T. (2000) Mineralogy, composition, and alteration of Mars Pathfinder rocks and soils: Evidence from multispectral, elemental, and magnetic data on terrestrial analogue, SNC meteorite, and Pathfinder samples. *Journal of Geophysical Research, Planets* **105**, 1757-1817.

Morrison, S.M., Downs, R.T., Blake, D.F., Vaniman, D.T., Ming, D.W., Hazen, R.M., Treiman, A.H., Achilles, C.N., Yen, A.S., Morris, R.V., Rampe, E.B., Bristow, T.F., Chipera, S.J., Sarrazin, P.C., Gellert, R., Fendrich, K.V., Morookian, J.M., Farmer, J.D., Des Marais, D.J., & Craig, P.I. (2018) Crystal chemistry of martian minerals from Bradbury Landing through Naukluft Plateau, Gale crater, Mars. *American Mineralogist* **103,** 857-871.

Mustoe, G.E. (1996) Hisingerite - A Rare Iron Mineral from Walker Valley, Skagit County, Washington. *Washington Geology* **24**, 14-19.

Nagasawa, K. (1978) Weathering of volcanic ash and other pyroclastic materials. In *Clay and Clay Minerals of Japan* (eds. T. Sudo and S. Shimoda). Elsevier Science Publishing Company, Amsterdam, pp. 105-125.

Nagy, K.L., Blum, A.E., & Lasaga A.C. (1991) Dissolution and precipitation kinetics of kaolinite at 80 °C and pH 3: the dependence on solution saturation state. *American Journal of Science* **291,** 649-696.

Ohashi, F., Wada, S.I., Suzuki, M., Maeda, M., & Tomura, S. (2002) Synthetic allophane from high-concentration solutions: nanoengineering of the porous solid. *Clay Minerals* **37**, 451-456.

Olsen, A.A., Hausrath, E.M., & Rimstidt, J.D. (2015) Forsterite dissolution rates in Mg-sulfate-rich Mars-analog brines and implications of the aqueous history of Mars. *Journal of Geophysical Research, Planets* **120**, 388-400.

Ossaka, J., Iwai, S.-i., Kasai, M., Shirai, T., & Hamada, S. (1971) Coexistence states of iron in synthesized iron-bearing allophane (Al2O3-SiO2-Fe2O3-H2O system), *Bulletin of the Chemical Society of Japan* **44**, 716-718.

Palandri, J.L. & Kharaka, Y.K. (2004) A compilation of rate parameters of water-mineral interaction kinetics for application to geochemical modeling. U.S. Geological Survey Water-Resources Investigations Report 04-1068.

Parfitt, R.L. (1990) Allophane in New Zealand - a review. *Australian Journal of Soil Research* **28**, 343.

Pickering, R. (2014) Tri-Octahedral Domains and Crystallinity in Synthetic Clays: Implications for Lacustrine Paleoenvironmental Reconstruction. Thesis, Georgia State University.

Potts, P.J., Webb, P.C., & Watson, J.S. (1984) Energy dispersive x-ray fluorescence analysis of silicate rocks for major and trace elements. *X-Ray Spectrometry* **13**, 2-15.

Rampe, E. B., Blake, D.F., Bristow, T.F., Ming, D.W., Vaniman, D.T., Morris, R.V., Achilles, C.N., Chipera, S.J., Morrison, S.M., Tu, V.M., Yen, A.S., Castle, N., Downs, G.W., Downs, R.T., Grotzinger, J.P., Hazen, R.M., Treiman, A.H., Peretyazhko, T.S., Des Marais, D.J., Walroth, R.C., Craig, P.I., Crisp, J.A., Lafuente, B., Morookian, J.M., Sarrazin, P.C., Thorpe, M.T., Bridges, J.C., Edgar, L.A., Fedo, C.M., Freissinet, C., Gellert, R., Mahaffy, P.R., Newsom, H.E., Johnson, J.R., Kah, L.C., Siebach, K.L., Schieber, J., Sun, V.Z., Vasavada, A.R., Wellington, D., Wiens, R.C., and the MSL Science Team (2020) Mineralogy and geochemistry of sedimentary rocks and eolian sediments in Gale crater, Mars: A review after six Earth years of exploration with Curiosity. *Geochemistry* **80**, 125605.

Rampe, E.B., Ming, D.W., Blake, D.F., Bristow, T.F., Chipera, S.J., Grotzinger, J.P., Morris, R.V., Morrison, S.M., Vaniman, D.T., Yen, A.S., Achilles, C.N., Craig, P.I., Des Marais, D.J., Downs, R.T., Farmer, J.D., Fendrich, K.V., Gellert, R., Hazen, R.M., Kah, L.C., Morookian, J.M., Peretyazhko, T.S., Sarrazin, P., Treiman, A.H., Berger, J.A., Eigenbrode, J., Fairén, A.G., Forni, O., Gupta, S., Hurowitz, J.A., Lanza, N.L., Schmidt, M.E., Siebach, K., Sutter, B., & Thompson L.M. (2017) Mineralogy of an ancient lacustrine mudstone succession from the Murray formation, Gale crater, Mars. *Earth and Planetary Science Letters* **471**, 172-185.

Rampe, E.B., Morris, R.V., Archer, P.D., Agresti, D.G., & Ming, D.W. (2016) Recognizing sulfate and phosphate complexes chemisorbed onto nanophase weathering products on Mars using in-situ and remote observations. *American Mineralogist* **101**, 678-689.

Rampe, E.B., Kraft, M.D., Sharp, T.G., Golden, D.C., Ming, D.W., & Christensen, P.R. (2012) Allophane detection on Mars with Thermal Emission Spectrometer data and implications for regional-scale chemical weathering processes. *Geology* **40**, 995-998.

Rampe, E.B., Kraft, M.D., Sharp, T.G., Golden, D.C., Ming, D.W., Christensen, P.R., & Ruff S.W. (2011) Detection of allophane on Mars through orbital and in-situ thermal infrared spectroscopy. *Lunar Planet. Sci. XLII.* Lunar Planet. Inst., Houston, #2145(abstr.).

Rimstidt, J.D. & Barnes, H.L. (1980) The kinetics of silica-water reactions. *Geochimica et Cosmochimica Acta* **44**, 1683-1700.

Rozalen, M.L., Huertas, F.J., Brady, P.V., Cama, J., García-Palma, S., & Linares, J. (2008) Experimental study of the effect of pH on the kinetics of montmorillonite dissolution at 25 °C. *Geochimica et Cosmochimica Acta* **72,** 4224-4253.

Shayan, A. (1984) Hisingerite Material from a Basalt Quarry near Geelong, Victoria, Australia. *Clays and Clay Minerals* **32**, 272-278.

Shayan, A. Sanders, J.V., & Lancucki, C.J. (1988) Hydrothermal alterations of hisingerite material from a basalt quarry near Geelong, Victoria, Australia. *Clays and Clay Minerals* **36,** 327-336.

Singer, R.B. (1985) Spectroscopic observation of Mars. *Advances in Space Research* **5**, 59-68.

Smith, R.J., Rampe, E.B., Horgan, B.H.N., & Dehouck, E. (2018) Deriving amorphous component abundance and composition of rocks and sediments on Earth and Mars. *Journal of Geophysical Research, Planets* **123,** 2485-2505.

Squyres, S.W., Arvidson, R.E., Ruff, S., Gellert, R., Morris, R.V., Ming, D.W., Crumpler, L., Farmer, J.D., Des Marais, D.J., Yen, A., McLennan, S.M., Calvin, W., Bell 3rd, J.F., Clark, B.C., Wang, A., McCoy, T.J., Schmidt, M.E., & de Souza Jr., P.A. (2008) Detection of silica-rich deposits on Mars. *Science* **320**, 1063-1067.

Steiner, M.H., Hausrath, E.M., Elwood-Madden, M.E., Tschauner, O., Ehlmann, B.L., Olsen, A.A., Gainey, S.R. & Smith, J.S. (2016) Dissolution of nontronite in chloride brines and implications for the aqueous history of Mars. *Geochimica et Cosmochimica Acta* **195**, 259-276.

Stillings, L.L. & Brantley, S.L. (1995) Feldspar dissolution at 25 °C and pH 3: reaction stoichiometry and the effect of cations. *Geochimica et Cosmochimica Acta* **59,** 1483-1496.

Sun, Z., Zhou, H., Glasby, G., Yang, Q., Yin, X., Li, J., & Chen, Z. (2011) Formation of Fe-Mn-Si oxide and nontronite deposits in hydrothermal fields on the Valu Fa Ridge, Lau Basin, *Journal of Asian Earth Sciences* **43**, 64-76.

Sutter, B., McAdam, A.C., Mahaffy, P.R., Ming, D.W., Edgett, K.S., Rampe, E.B., Eigenbrode, J.L., Franz, H.B., Freissinet, C., Grotzinger, J.P., Steele, A., House, C.H., Archer, P.D., Malespin, C.A., Navarro-González, R., Stern, J.C., Bell, J.F., Calef, F.J., Gellert, R., Glavin, D.P., Thompson, L.M., & Yen, A.S. (2017) Evolved gas analyses of sedimentary rocks and eolian sediment in Gale crater, Mars: Results of the Curiosity rover's sample analysis at Mars instrument from Yellowknife Bay to the Namib Dune. *Journal of Geophysical Research, Planets* **122**, 2574-2609.

Theng, B.K.G., Russell, M., Churchman, G.J., & Parfitt, R.L. (1982) Surface properties of allophane, halloysite, and imogolite. *Clays and Clay Minerals* **30**, 143-149.

Tosca, N.J., Knoll, A.H., & McLennan, S.M. (2008) Water Activity and the Challenge for Life on Early Mars. *Science* **320**, 1204-1207.

Treiman, A.H., Bish, D.L., Vaniman, D.T., Chipera, S.J., Blake, D.F., Ming, D.W., Morris, R.V., Bristow, T.F., Morrison, S.M., Baker, M.B., Rampe, E.B., Downs, R.T., Filiberto, J., Glazner, A.F., Gellert, R., Thompson, L.M., Schmidt, M.E., Le Deit, L., Wiens, R.C., McAdam, A.C., Achilles, C.N., Edgett, K.S., Farmer, J.D., Fendrich, K.V., Grotzinger, J.P., Gupta, S., Morookian, J.M., Newcombe, M.E., Rice, M.S., Spray, J.G., Stolper, E.M., Sumner, D.Y., Vasavada, A.R., & Yen, A.S. (2016). Mineralogy, provenance, and diagenesis of a potassic basaltic sandstone on Mars: CheMin X-ray diffraction of the Windjana sample (Kimberley area, Gale Crater). *Journal of Geophysical Research, Planets* **121**(1), 75-106.

Tu, V.M., Hausrath, E.M., Tschauner, O., Iota, V., & Egeland, G.W. (2014) Dissolution rates of amorphous Al- and Fe-phosphates and their relevance to phosphate mobility on Mars. *Americal Mineralogist* **99**, 1206-1215.

Van der Gaast, S.J. & Vaars, A.J. (1981) A Method to Eliminate the Background in X-Ray-Diffraction Patterns of Oriented Clay Mineral Samples. *Clay Minerals* **16**, 383-393.

Vaniman, D.T., Bish, D.L., Ming, D.W., Bristow, T.F., Morris, R.V., Blake, D.F., Chipera, S.J., Morrison, S.M., Treiman, A.H., Rampe, E.B., Rice, M., Achilles, C.N., Grotzinger, J.P., McLennan, S.M., Williams, J., Bell 3rd, J.F., Newsom, H.E., Downs, R.T., Maurice, S., Sarrazin, P., Yen, A.S., Morookian, J.M., Farmer, J.D., Stack, K., Milliken, R.E., Ehlmann, B.L., Sumner, D.Y., Berger, G., Crisp, J.A., Hurowitz, J.A., Anderson, R., Des Marais, D.J., Stolper, E.M., Edgett, K.S., Gupta, S., Spanovich, N., & the MSL Science Team (2014) Mineralogy of a mudstone at Yellowknife Bay, Gale crater, Mars. *Science* **343**, 1243480.

Velbel, M.A. (1993) Constancy of silicate-mineral weathering-rate ratios between natural and experimental weathering: implications for hydrologic control of differences in absolute rates. *Chemical Geology* **105,** 89-99.

Wada, K. (1989) Allophane and Imogolite. In: *Minerals in Soil Environments* (eds. J. B. Dixon and S. B. Weed). Soil Science Society of America, Madison, Wisconsin, USA, pp. 1051-1087.

Wada, K. & Yoshinaga, N. (1969) The structure of imogolite. *American Mineralogist* **54**, 50-71.

Weitz, C.M., Bishop, J.L., Baker, L.L., & Berman, D.C. (2014) Fresh exposures of hydrous Fe-bearing amorphous silicates on Mars. *Geophysical Research Letters* **41**, 8744-8751.

Welch, S.A. & Ullman, W.J. (2000) The temperature dependence of bytownite feldspar dissolution in neutral aqueous solutions of inorganic and organic ligands at low temperature (5–35°C). *Chemical Geology* **167**, 337-354.

Wogelius, R.A. & Walther, J.V. (1991) Olivine dissolution at 25 °C: effects of pH, CO2, and organic acids. *Geochimica et Cosmochimica Acta* **55**(4), 943-954.

Yen, A.S., Ming, D.W., Vaniman, D.T., Gellert, R., Blake, D.F., Morris, R.V., Morrison, S.M., Bristow, T.F., Chipera, S.J., Edgett, K.S., Treiman, A.H., Clark, B.C., Downs, R.T., Farmer, J.D., Grotzinger, J.P., Rampe, E.B., Schmidt, M.E., Sutter, B., & Thompson, L.M. (2017) Multiple stages of aqueous alteration along fractures in mudstone and sandstone strata in Gale crater, Mars. *Earth and Planetary Science Letters* **471**, 186-198.

Zhu, C., Liu, Z., Zhang, Y., Wang, C., Scheafer, A., Lu, P., Zhang, G., Georg, R.B., Yuan, H., & Rimstidt, J.D. (2016) Measuring silicate mineral dissolution rates using Si isotope dating. *Chemical Geology* **445,** 146-163.

FIGURE CAPTIONS

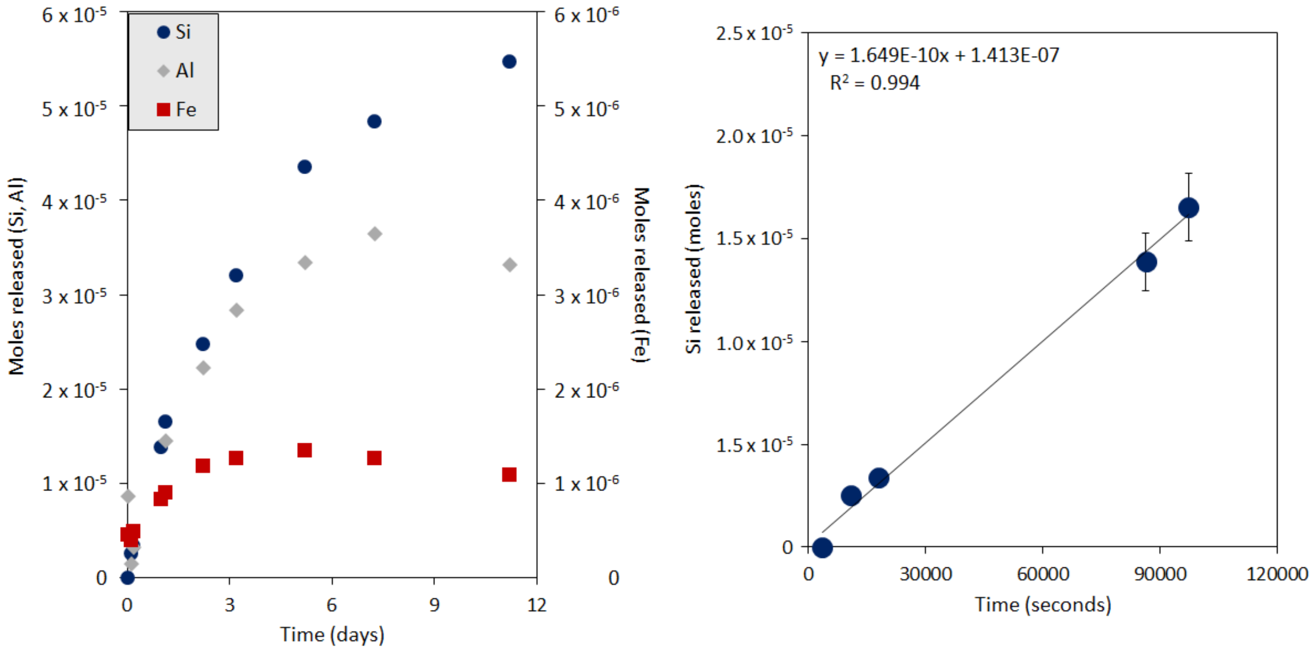

Fig. 1 Representative solution chemistry data for a dissolution experiment. **(a)** Typical shape of the Si, Al, and Fe release curves for Fe-free allophane, Fe-poor allophane, and Fe-rich allophane dissolution (note the difference in scale between Si and Al released versus Fe released). **(b)** The linear portion of the silica release curve as exemplified by a pH_0_3_FRA experiment. The linear portion of the silica release curve was fit with a linear regression (equation and R^2 value shown). Error bars are the standard error of the AA measurement, and are smaller than the points for the first three points. In general, Fe-rich allophane reached higher final Si, Al, and Fe concentrations than Fe-free allophane or Fe-poor allophane (**Fig. S9-S14**). No Al or Fe release was observed in experiments at pH_0 5, 7, or 10. Fe release was only observed in Fe-rich allophane experiments at pH_0 3. All data for all experiments are given in the supplemental material (**Data sheets S1-S38**)

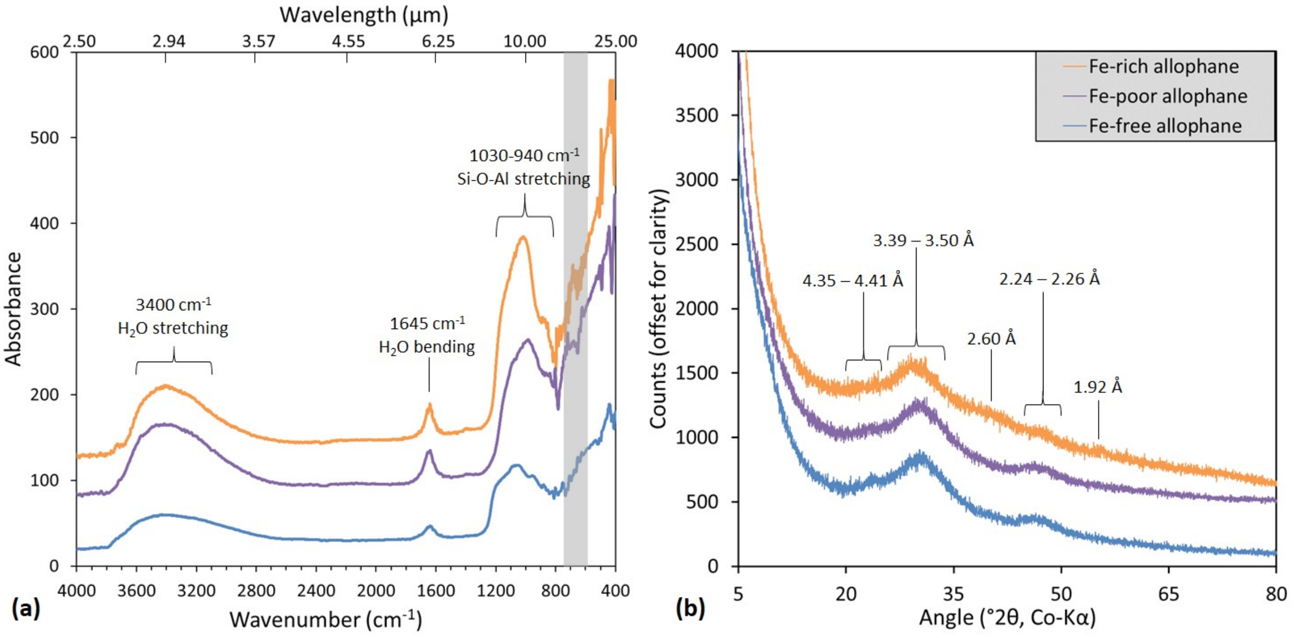

Fig. 2 FTIR-PAS absorption spectra **(a)** and XRD patterns **(b)** of unreacted synthetic Fe-free allophane, Fe-poor allophane, and Fe-rich allophane. **(a)** FTIR-PAS absorption spectra of synthetic Fe-free allophane, Fe-poor allophane, and Fe-rich allophane. All samples had absorption bands at 3400 cm^{-1}, 1645 cm^{-1}, 1030 cm^{-1}, and 940 cm^{-1} (labeled), and a weak band near 620 cm^{-1} (shaded box), in agreement with literature values for allophane and hisingerite. The spectra are offset for clarity. **(b)** Unreacted synthetic Fe-rich allophane, Fe-poor allophane, and Fe-free allophane. In the Fe-rich allophane sample, a broad peak, indicative of nano-crystalline structure, is visible around 3.50 Å (29.6°2θ), with minor broad peaks at 2.60, 2.24, and 1.92 Å (40.2, 47.1, and 55.5°2θ, respectively). In the Fe-poor allophane sample, peaks occur at 4.41, 3.42, and 2.26 Å (23.4, 30.3, and 46.6°2θ). In the Fe-free allophane sample, broad peaks occur at 4.35, 3.39, and 2.25 Å (23.7, 30.6, and 46.8°2θ). All samples show elevated low background indicative of small particle sizes. Co Kα radiation was used for all patterns

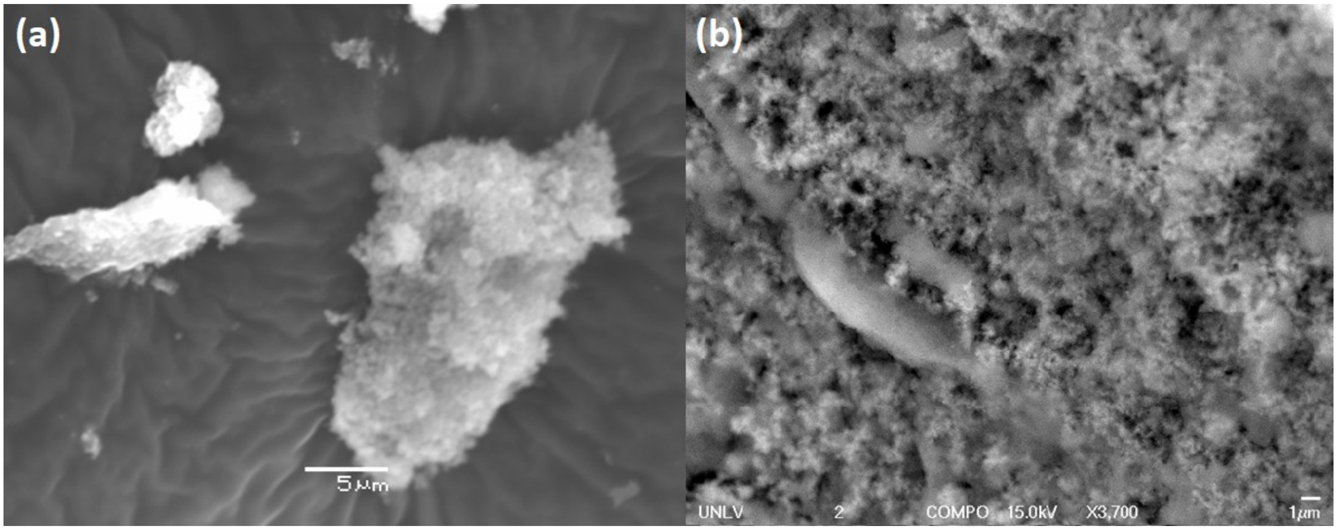

Fig. 3 Synthetic Fe-rich allophane imaged by SEM **(a)** and FE-SEM **(b)**. Nano-spherules are distinguishable in the "fluffy" texture of the aggregate. Similar textures were observed in Fe-free allophane and Fe-poor allophane samples (**Fig. S6-S7**, supplemental material). The long, apparently smooth object in **(b)** is a ridge of "fluffy" material that is out of focus

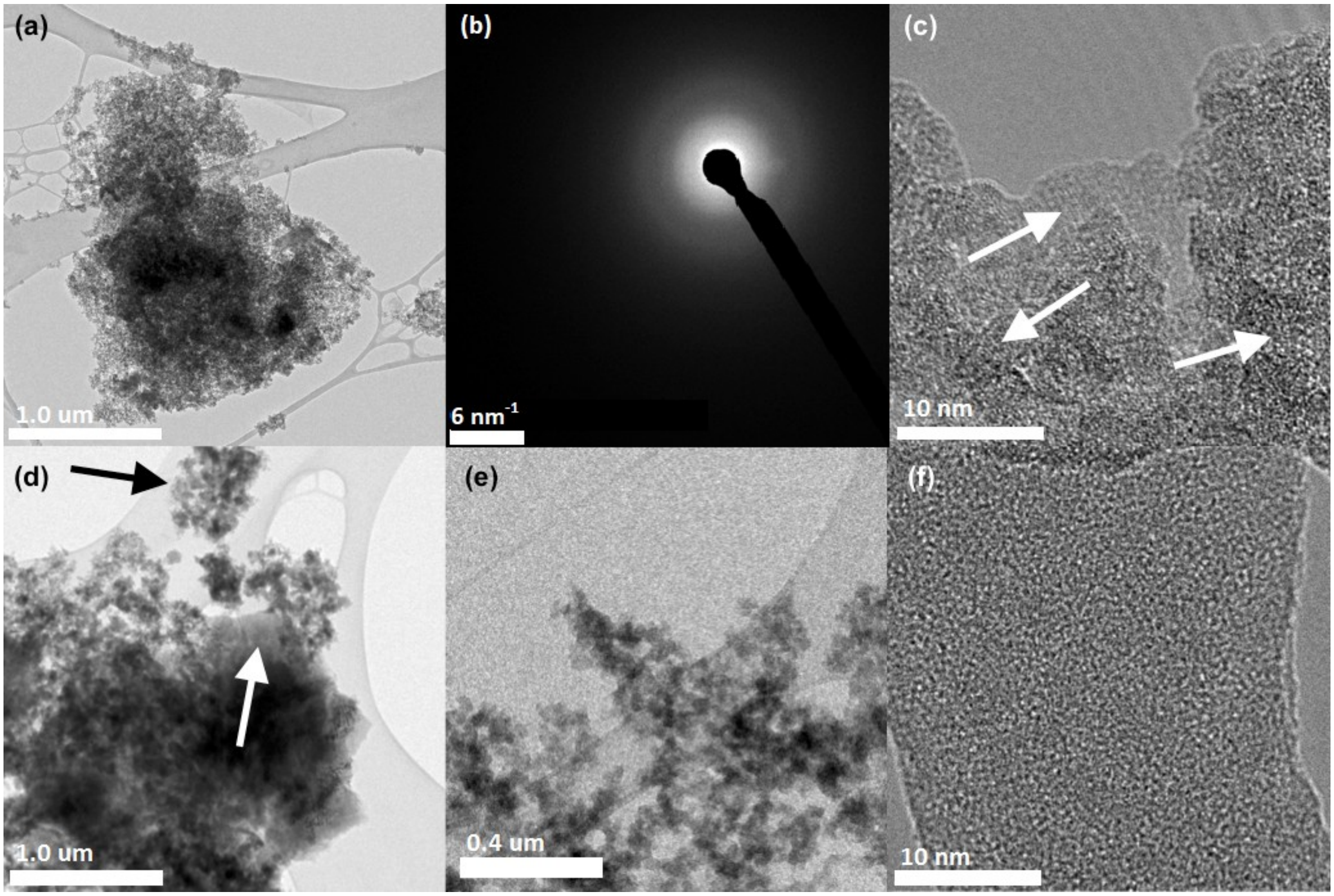

Fig. 4 FE-STEM images of synthetic Fe-rich allophane **(a-c)** and Fe-free allophane **(d-f)**. **(a)** An agglomerate of synthetic Fe-rich allophane. **(b)** Diffraction pattern from an agglomerate of unaltered synthetic Fe-rich allophane, obtained during TEM investigations. Diffuse rings are visible, indicating nanocrystalline structure. Diffractograms were not obtained for synthetic Fe-free allophane due to its lack of lattice fringes, indicating no long-range order. **(c)** A very high-magnification view of synthetic Fe-rich allophane. Lattice fringes (arrows) indicate some crystalline structure. **(d)** An agglomerate of synthetic Fe-free allophane. Nano-spherule-like structures are visible along the edges of the agglomerate. Both the "rugged" (black arrow) and "blobby" (white arrow) textures are visible. **(e)** A closer view of **(d)**, showcasing the "rugged" nano-spherule structures. **(f)** Very high magnification of synthetic Fe-free allophane. Note the lack of lattice fringes, indicating no long-range crystal structure

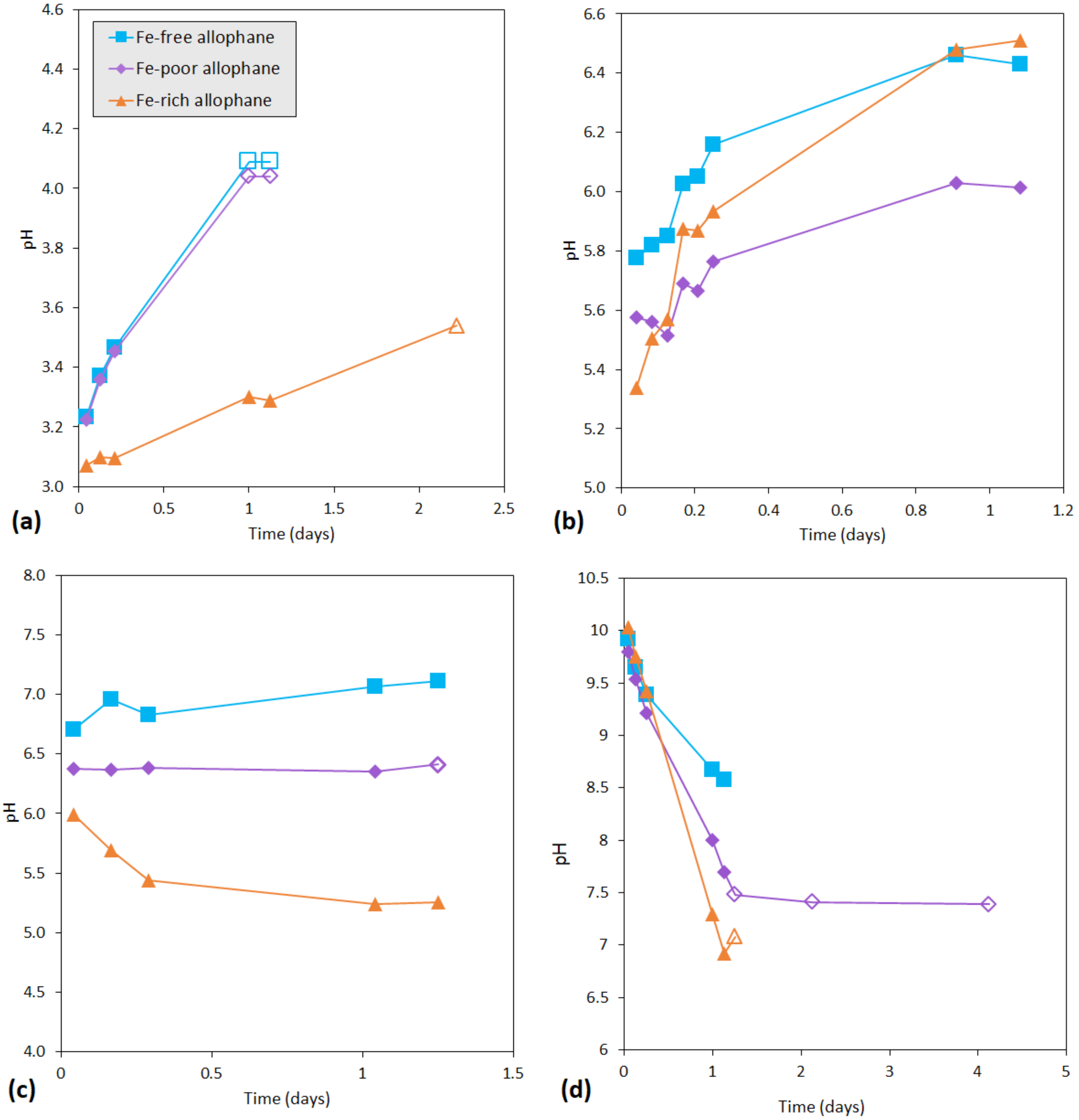

Fig. 5 Observed change in solution pH with time over the range used to calculate dissolution rates for experiments with pH_0 3 **(a)**, pH_0 5 **(b)**, pH_0 7 **(c)**, and pH_0 10 **(d)**. Points are the average pH value between two duplicates. Solution pH was measured over the course of the entire experiments (see **Fig. S8**). Balanced chemical equations (see supplemental material Section S8) explain the observed pH changes

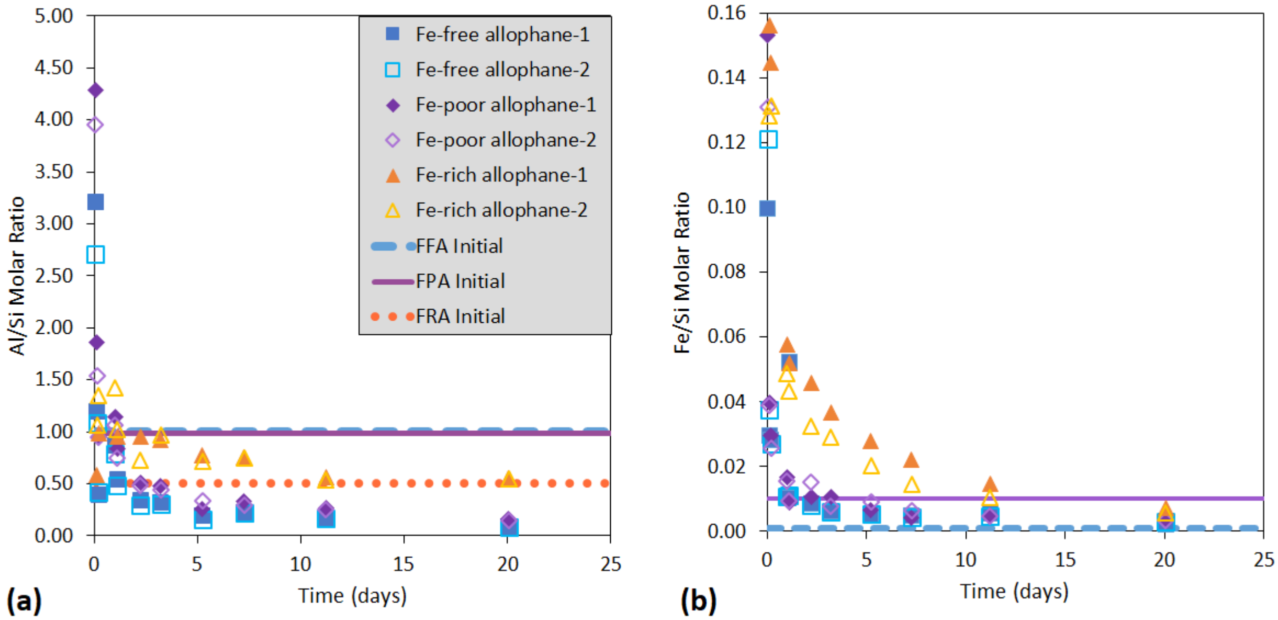

Fig. 6 Al/Si ratio **(a)** and Fe/Si ratio **(b)** measured from solution in pH$_0$ 3 experiments versus time. Points where Fe, Al, or Si were below detection are not plotted. The formula ratios of the unaltered Fe-free allophane (FFA), Fe-poor allophane (FPA), and Fe-rich allophane (FRA) are indicated by FFA Initial, FPA Initial, and FRA Initial, respectively. In panel **(b)**, the Fe/Si synthesis ratio of the unaltered Fe-rich allophane is 0.5, well above any of the measured ratios in our solutions

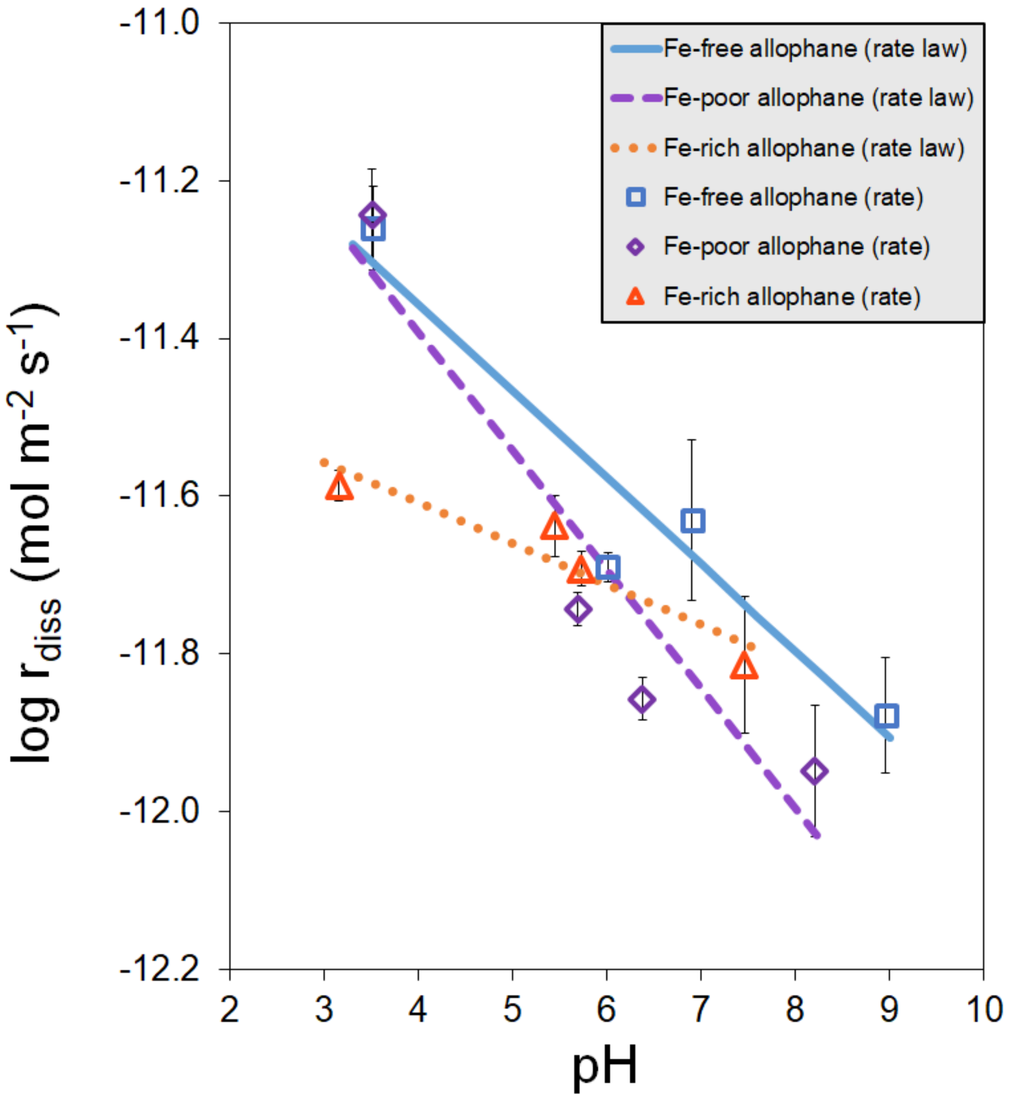

Fig. 7 Average of the dissolution rates (points) and rate laws calculated as described in the text (lines) for Fe-free allophane, Fe-poor allophane, and Fe-rich allophane at pH$_0$ values of 3, 5, 7, and 10. Error bars represent the 1-σ standard deviation between duplicate experiments. Overall, the pH-dependence of dissolution was low. All experimental data are given in the supplemental material

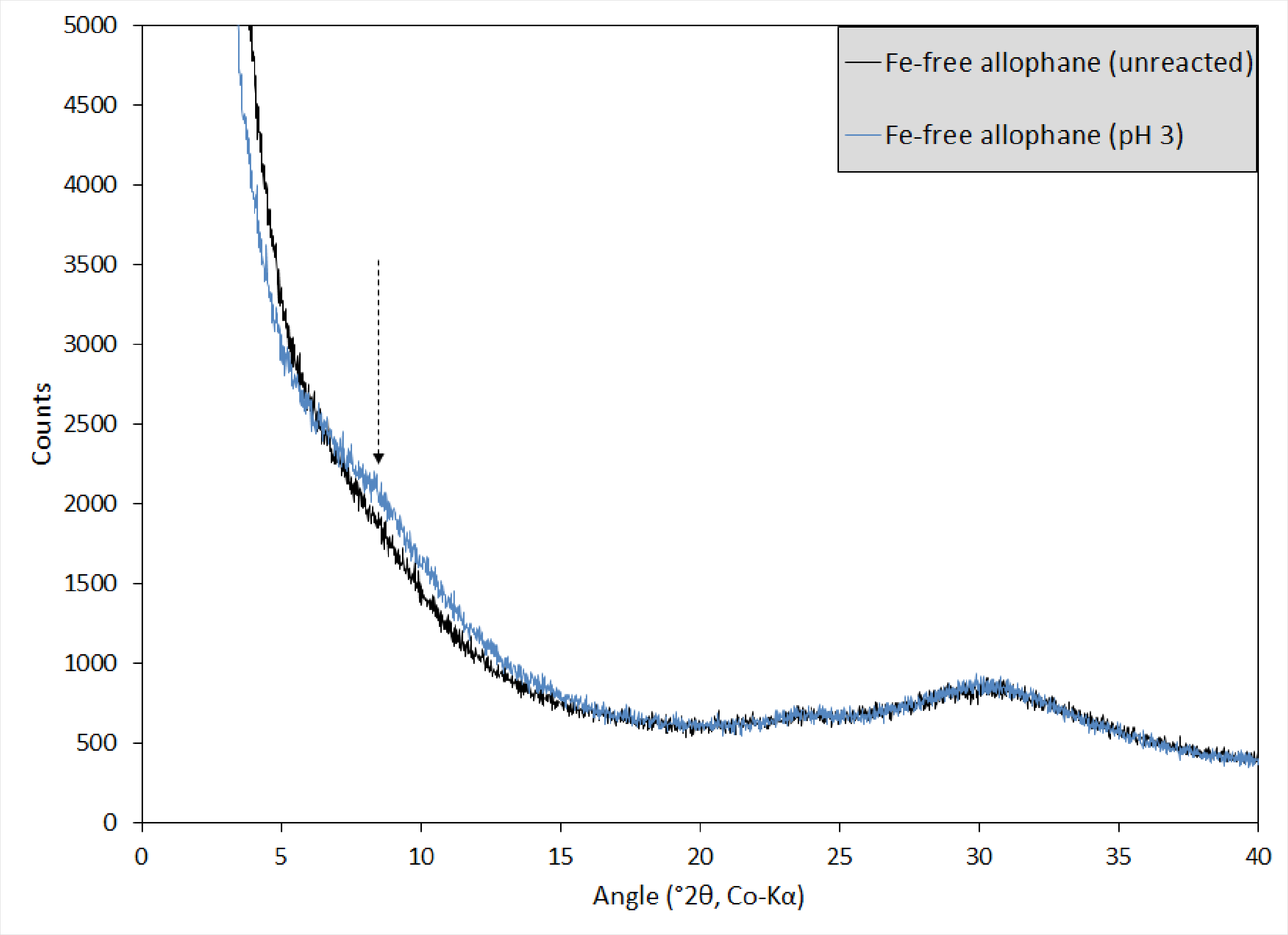

Fig. 8 XRD patterns of unreacted Fe-free allophane and Fe-free allophane reacted at pH_0 3 (pH_0_3_FFA), demonstrating the development of a possible phyllosilicate-like precursor phase (arrow) with a peak centered around 12.3 Å. A similar, but less pronounced, feature was observed in Fe-free allophane samples reacted at pH_0 7 and 10; in Fe-poor allophane reacted at pH_0 3; and in Fe-rich allophane reacted at pH_0 10. XRD patterns of all unreacted and reacted materials were collected (see **Fig. S15**). Co Kα radiation was used for all patterns

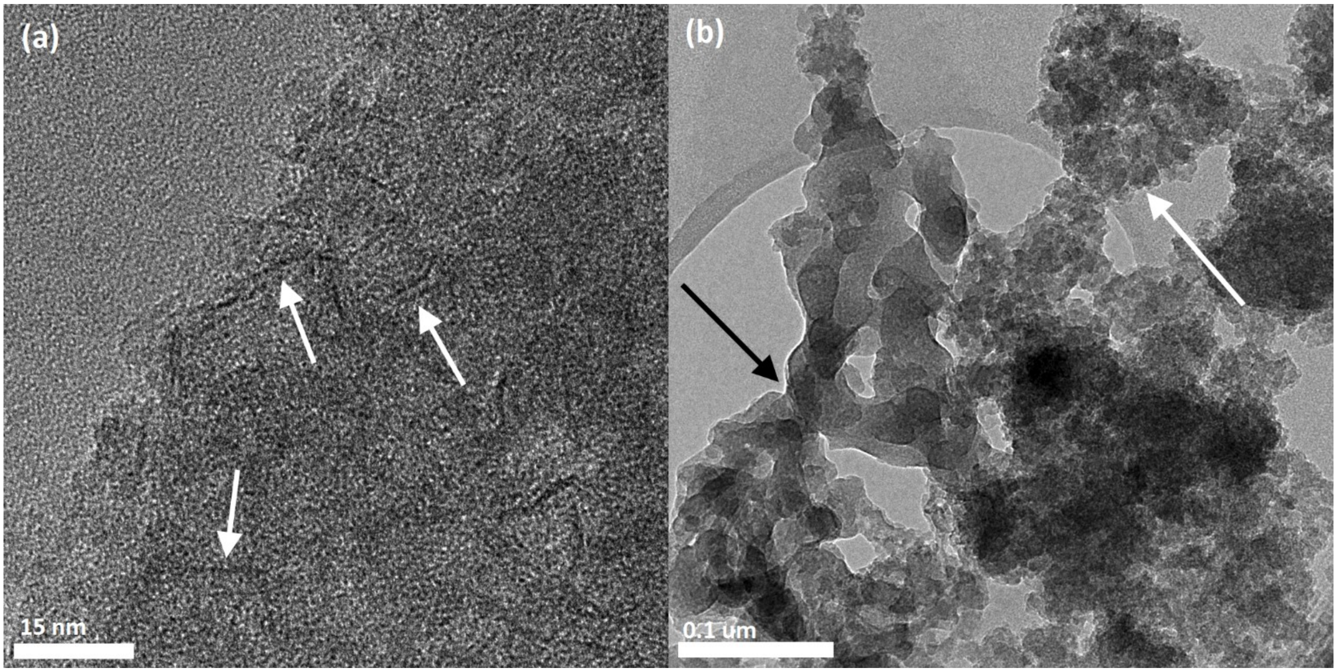

Fig. 9 FE-STEM images of synthetic Fe-rich allophane **(a)** and Fe-free allophane **(b)**, each reacted at pH_{steady} values of ~8 (pH_0 10) for 57 d. Edge-curl features were much less prevalent in the Fe-free allophane sample than in the Fe-rich allophane (see **Fig. S20**, supplemental material, for an example of an edge-curl feature in the Fe-free allophane). **(a)** Arrows indicate linear features that may represent the curled edges of incipient phyllosilicate-like sheets. **(b)** The "blobby" morphology is visible on the left (black arrow), while the "rugged" morphology is on the right (white arrow)

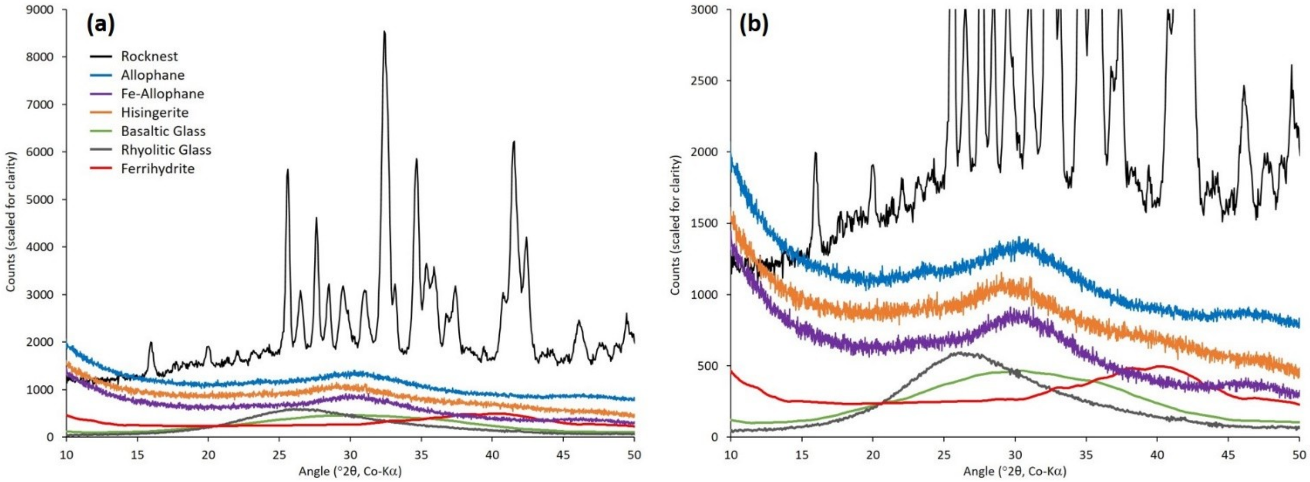

Fig. 10 Comparison of the XRD patterns of synthetic Fe-free allophane, Fe-poor allophane, and Fe-rich allophane with a 2-line ferrihydrite from the FULLPAT library and the CheMin XRD pattern from the Rocknest soil sample. Panel **(a)** shows the full patterns, and panel **(b)** is zoomed in to better demonstrate the concordance between our amorphous materials and the amorphous humps in the Rocknest pattern. Co Kα radiation was used for all patterns

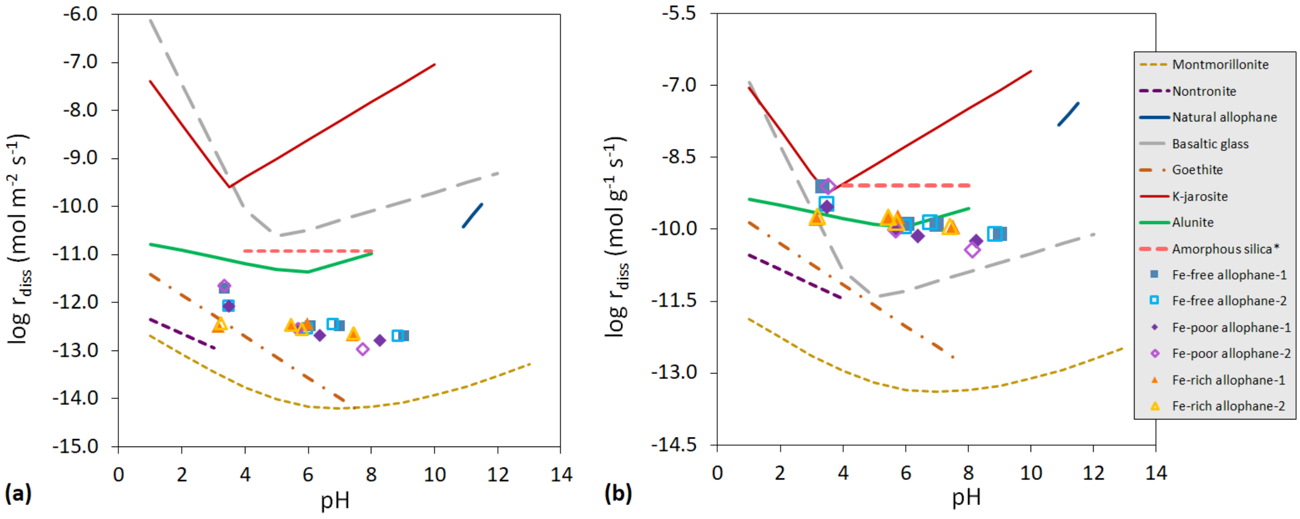

Fig. 11 Comparison of the log of the surface area-normalized **(a)** and mass-normalized **(b)** dissolution rates of our synthetic Fe-free allophane, Fe-poor allophane, and Fe-rich allophane at 25°C (points) with rate laws for montmorillonite (Rozalen et al. 2008), nontronite (Gainey et al. 2014), natural allophane (Abidin et al. 2004), basaltic glass (Gislason and Oelkers. 2003), goethite (Cheah et al. 2003), K-jarosite (Elwood-Madden et al. 2012), alunite (Miller et al. 2016), and amorphous silica* (Rimstidt and Barnes, 1980) (lines) *modified to reflect elevated dissolution rates in 0.01 M NaCl as per Icenhower et al. (2000) in order to make a more direct comparison to the conditions of our dissolution experiments. Slower dissolution rates of allophane relative to glass and jarosite in panel **(a)** may be impacted by the very large surface areas of Fe-free allophane (BET SSA ≈ 386 m^2 g^{-1}), Fe-poor allophane (BET SSA ≈ 350 m^2 g^{-1}), and Fe-rich allophane (BET SSA ≈ 507 m^2 g^{-1}), as evidenced by the mass-normalized rates shown in panel **(b)**. Error bars are smaller than the points

TABLES

Table 1. Synthesis recipes, Al:Fe:Si molar ratios, BET SSA and particle sizes for Fe-free allophane, Fe-poor allophane, and Fe-rich allophane. NaOH was used to hydrolyze TEOS to allow Si to bind with Al and Fe.

Material	**0.1 M $AlCl_3$ (mL)**	**0.1 M $FeCl_3$ (mL)**	**TEOS (mL)**	**1 M NaOH (mL)**	**Al:Fe:Si molar ratio***	**BET SSA ($m^2\ g^{-1}$)**	**Particle size (µm)**
Fe-free allophane	167.00	0.00	3.72	50.00	1:0:1	385.77 ± 0.15	167.5 ± 2.2
Fe-poor allophane	165.33	1.67	3.72	50.00	0.99:0.01:1	350.24 ± 10.67	133.1 ± 0.8
Fe-rich allophane	83.5	83.5	3.72	50.00	0.5:0.5:1	507.48 ± 0.22	166.5 ± 4.9

*Synthesis ratios. The compositions of the final solids measured via total digestion were slightly more Al-rich than the synthesis ratios (**Table 6**).

Table 2. Table of dissolution experiments. *NA* = none added.

Experiment name	**Material**	**Starting solution**	**Initial pH (pH_0)**	**Starting mass (mg)**
pH_0_3_FFA	Fe-free allophane	0.01 M NaCl + HNO_3	3.01	150.00 ± 0.10
pH_0_3_FPA	Fe-poor allophane	0.01 M NaCl + HNO_3	3.01	150.25 ± 0.05
pH_0_3_FRA	Fe-rich allophane	0.01 M NaCl + HNO_3	3.01	149.95 ± 0.35
pH_0_3_BLANK	*NA*	0.01 M NaCl + HNO_3	3.01	0
pH_0_5_FFA	Fe-free allophane	0.01 M NaCl + HNO_3	5.04	149.85 ± 0.25
pH_0_5_FPA	Fe-poor allophane	0.01 M NaCl + HNO_3	5.04	149.85 ± 0.05
pH_0_5_FRA	Fe-rich allophane	0.01 M NaCl + HNO_3	5.04	149.85 ± 0.25
pH_0_5_BLANK	*NA*	0.01 M NaCl + HNO_3	5.04	0
pH_0_7_FFA	Fe-free allophane	0.01 M NaCl + NaOH	6.99	150.10 ± 0.10
pH_0_7_FPA	Fe-poor allophane	0.01 M NaCl + NaOH	6.99	150.2*
pH_0_7_FRA	Fe-rich allophane	0.01 M NaCl + NaOH	6.99	149.80 ± 0.10
pH_0_7_BLANK	*NA*	0.01 M NaCl + NaOH	6.99	0
pH_0_10_FFA	Fe-free allophane	0.01 M NaCl + NaOH	10.36	150.30 ± 0.10
pH_0_10_FPA	Fe-poor allophane	0.01 M NaCl + NaOH	10.36	149.95 ± 0.35
pH_0_10_FRA	Fe-rich allophane	0.01 M NaCl + NaOH	10.36	150.00 ± 0.30
pH_0_10_BLANK	*NA*	0.01 M NaCl + NaOH	10.36	0

*Duplicate experiment excluded because of low mass (73.7 mg), high standard error, and poor R^2 value (**Data Sheet S18**).

Table 3. pH at the first time point (t_i) and at the final time point (t_f) of the data used to calculate the dissolution rates, the dissolution rates (r_{diss}) and their 1-σ standard deviations (Std err). The "-1" or "-2" suffix indicates duplicate experiments. Averages of the data are plotted in **Fig. 7** with rate laws calculated as described in the text. Cells in italics were omitted from the rate law calculation due to anomalous experimental conditions (see supplemental material **Data Sheet S18**). All solution compositions for each experiment at each time point are given in supplemental material (**Data Sheets S1-S38**).

Material	**pH 3**				**pH 5**				**pH 7**				**pH 10**			
	pH at t_i	**pH at t_f**	**r_{diss}[a] x 10^{-12}**	**Std err[a] x 10^{-12}**	**pH at t_i**	**pH at t_f**	**r_{diss} x 10^{-12}**	**Std err x 10^{-12}**	**pH at t_i**	**pH at t_f**	**r_{diss} x 10^{-12}**	**Std err x 10^{-12}**	**pH at t_i**	**pH at t_f**	**r_{diss} x 10^{-12}**	**Std err x 10^{-12}**
Fe-free allophane-1	3.25	3.48	13.0	0.438	5.84	6.47	2.17	0.144	6.76	7.17	2.11	0.254	9.94	8.70	1.35	0.145
Fe-free allophane-2	3.22	4.09	5.57	0.435	5.77	6.39	2.05	0.103	6.65	7.06	2.28	0.356	9.90	8.46	1.30	0.172
Fe-poor allophane-1	3.21	4.04	5.70	0.423	5.59	5.98	1.95	0.101	6.38	6.40	1.39	0.0846	9.81	7.80	1.09	0.172
Fe-poor allophane-2	3.24	3.48	14.7	2.75	5.55	6.05	1.88	0.119	*6.37*	*6.35*	*1.49*	*0.936*	9.78	7.39	0.716	0.0719
Fe-rich allophane-1	3.07	3.23	2.17	0.0995	5.63	6.56	2.41	0.104	5.94	5.27	2.29	0.158	10.04	7.08	1.45	0.138
Fe-rich allophane-2	3.07	3.54	2.48	0.203	5.50	6.46	1.85	0.226	6.05	5.24	2.31	0.132	10.03	6.85	1.50	0.265

[a] r_{diss} and standard error have units of mol m^{-2} s^{-1}

Table 4. Summary of characterizations of altered synthetic materials. *NA* = No analysis performed. The different durations for experiments with different pH$_0$ values allowed all experiments to reach steady-state regardless of dissolution rate.

Method	**Fe-free allophane**			**Fe-poor allophane**			**Fe-rich allophane**		
	pH$_0$	pH$_{final}$	Duration (d)	pH$_0$	pH$_{final}$	Duration (d)	pH$_0$	pH$_{final}$	Duration (d)
SEM	*NA*	*NA*	*NA*	*NA*	*NA*	*NA*	3.02	5.35	2
							3.02	6.54	31
FE-STEM	10.36	8.59	57	*NA*	*NA*	*NA*	3.01	4.78	181
							10.36	6.39	57
XRD	3.01	4.42	20	3.01	4.35	20	3.01	3.97	20
	5.04	6.85	12	5.04	6.37	12	5.04	7.06	12
	6.99	7.20	93	6.99	6.40	93	6.99	5.00	93
	10.36	7.79	18	10.36	7.18	12	10.36	6.56	12
Total digestion	3.01	4.42	20	3.01	4.35	20	3.01	3.97	20
	5.04	6.85	12	5.04	6.37	12	5.04	7.06	12
	6.99	7.20	93	6.99	6.40	93	6.99	5.00	93
	10.36	7.79	18	10.36	7.18	18	10.36	6.56	18

Table 5. A summary of the peak positions observed in various natural and synthetic allophane and hisingerite samples. **Table 8** gives peak positions for all materials, unreacted and reacted, examined in this study. Data for Allophane from Wada and Yoshinaga (1969). Data for Al-rich allophane from Parfitt (2009). Data for Synthetic allophane from Rampe et al. (2012). Data for iron-coprecipitated allophane from Ossaka et al. (1971). Data for Hisingerite from Henmi et al. (1980). Data for Hisingerite from Geelong, Victoria, Australia from Shayan et al. (1988). Data for Hisingerite from Riddarhyttan, Sweden and Gillinge, Sweden from Eggleton and Tilley (1998). Data for Hisingerite from Indiana University collection from Milliken and Bish (2014). Data for synthetic nontronites incubated at 150°C and 95°C from Baker and Strawn (2014).

Sample	**Peak positions (Å)**								
Allophane				3.3		2.25			
Al-rich allophane	12		4.3	3.4		2.2	1.9	1.7	
Synthetic allophane				3.5		2.2		1.4	
Unreacted synthetic Fe-free allophane (this study)	12.27		4.35	3.39		2.25			
Iron-coprecipitated allophane				3.56					
Unreacted synthetic Fe-poor allophane (this study)			4.41	3.42		2.26			
Hisingerite			4.4	3.5	2.5-2.6			1.4-1.5	
Hisingerite from Geelong, Victoria, Australia			4.49		2.58				
Hisingerite from Riddarhyttan, Sweden		7.70	4.44	3.57	2.56	2.26	1.69	1.54	
Hisingerite from Gillinge, Sweden		7.51	4.41	3.58	2.57	2.41	1.68	1.54	1.32
Hisingerite from Indiana University collection			4.4	3.6	2.6			1.5	
Synthetic nontronite, 150°C incubated	11.8			3.8	2.7	2.2			
Synthetic nontronite, 95°C incubated	11.8			3.8					
Unreacted synthetic Fe-rich allophane (this study)				3.50	2.60	2.24	1.92		

Table 6. Compositions in wt.% oxide of unaltered and altered Fe-free allophane, Fe-poor allophane, and Fe-rich allophane determined by ICP-MS analysis of total digestion products (for SiO_2, Al_2O_3, and Fe_2O_3) and thermal gravimetric analysis (TGA; for H_2O) compared with samples from the literature and the approximate values expected from the chemical formulas. Error in the "formula" phases was determined by comparing variable Si, Al, Fe, and H_2O contents in endmember compositions. Error in the analyzed samples represents the standard deviation between two runs of each sample. TGA was not conducted on altered samples because insufficient sample mass was available for analysis. Comparisons of the composition of each unaltered synthetic material with multiple samples from the literature are given in **Tables S3-S5**. "ND" = Not Detected. Data for Silica Springs from Theng et al. (1982). Data for Kanumatsuchi from Kitagawa (1974). Data for Hisinger from Hisinger (1928).

Sample	**SiO_2**	**Al_2O_3**	**Fe_2O_3**	**H_2O**	**Sum**
Fe-free allophane (formula)	39.1 ± 6.0	41.0 ± 4.1	0	19.9 ± 2.6	100 ± 7.7
Silica Springs	33.4	43.8	0.28		
Unaltered allophane	30.2 ± 1.0	32.2 ± 0.8	*ND*	36.2 ± 1.0	98.6 ± 1.6
pH$_0$_3_FFA	30.4 ± 0.6	36.6 ± 0.9	*ND*		
pH$_0$_5_FFA	30.5 ± 0.2	31.9 ± 0.6	*ND*		
pH$_0$_7_FFA	30.2 ± 1.3	38.3 ± 1.5	*ND*		
pH$_0$_10_FFA	29.9 ± 0.2	37.4 ± 0.3	*ND*		
Fe-poor allophane (formula)	39.0 ± 6.0	40.5 ± 4.0	0.64 ± 0.06	19.8 ± 2.5	99.9 ± 7.6
Kanumatsuchi	29.17	33.81	0.56		
Unaltered Fe-allophane	29.6 ± 0.7	28.0 ± 0.9	0.47 ± 0.01	36.8 ± 1.0	94.9 ± 1.5
pH$_0$_3_FPA	28.9 ± 0.6	33.3 ± 0.9	0.48 ± 0.02		
pH$_0$_5_FPA	30.4 ± 1.1	30.0 ± 0.4	0.44 ± 0.01		
pH$_0$_7_FPA	28.2 ± 1.0	41.4 ± 0.9	0.39 ± 0.02		
pH$_0$_10_FPA	30.1 ± 0.6	37.2 ± 0.2	0.43 ± 0.01		
Fe-rich allophane (formula)	35.1 ± 5.7	18.4 ± 1.6	28.7 ± 2.6	17.8 ± 2.2	100 ± 6.8
Hisinger	27.5	5.5	51.5		
Unaltered Fe-rich allophane	30.2 ± 0.4	17.5 ± 0.3	19.3 ± 0.5	33.4 ± 1.1	100.4 ± 1.3
pH$_0$_3_FRA	28.1 ± 0.6	16.5 ± 0.1	19.7 ± 0.3		
pH$_0$_5_FRA	28.8 ± 0.9	18.5 ± 0.7	19.4 ± 0.1		
pH$_0$_7_FRA	27.2 ± 0.7	16.8 ± 0.7	19.2 ± 0.5		
pH$_0$_10_FRA	28.5 ± 1.0	17.4 ± 0.4	19.3 ± 0.3		

Table 7. Particle lifetimes for Fe-free allophane, Fe-poor allophane, and Fe-rich allophane calculated with *Eq. (4)*. The molar volume of all allophanes was assumed to be 1.01 x 10^{-4} m^2 mol^{-1}. Error (where given) represents the 1-σ standard deviation between duplicates.

Experimental condition	**Average r_{diss} at 25 °C x 10^{-12} (mol m^{-2} s^{-1})**	**Particle size (μm)**	**Particle lifetime (kyr)**
pH$_0$_3_FFA	9.30 ± 3.74	1.00	0.020 ± 0.008
		167.5 ± 2.2	3.35 ± 1.35
pH$_0$_3_FPA	10.20 ± 4.50	1.00	0.019 ± 0.008
		133.1 ± 0.8	2.53 ± 1.12
pH$_0$_3_FRA	2.33 ± 0.15	1.00	0.067 ± 0.004
		166.5 ± 4.9	11.226 ± 0.82
pH$_0$_10_FFA	1.32 ± 0.02	1.00	0.118 ± 0.002
		167.5 ± 2.2	19.747 ± 0.417
pH$_0$_10_FPA	0.95 ± 0.19	1.00	0.180 ± 0.038
		133.1 ± 0.8	24.008 ± 5.020
pH$_0$_10_FRA	1.48 ± 0.02	1.00	0.106 ± 0.002
		166.5 ± 4.9	17.598 ± 0.586

Table 8. Calculated peak positions for unreacted Fe-free allophane, Fe-poor allophane, and Fe-rich allophane, and for the altered materials from experiments with pH$_0$ values of 3, 5, 7, and 10. Numbers in italics are from minor peaks.

Material	**Peak positions (Å)**					
Unaltered allophane	*12.27*	4.35	3.39		2.25	
pH$_0$_3_FFA	11.72	4.37	3.42		2.26	
pH$_0$_5_FFA	*23.7*		3.41		2.25	
pH$_0$_7_FFA*	10.82	4.32	3.39		2.27	
pH$_0$_10_FFA	11.62	4.29	3.38		2.26	
Unaltered Fe-allophane		4.41	3.42		2.26	
pH$_0$_3_FPA	11.07		3.39		2.25	
pH$_0$_5_FPA			3.41		2.25	
pH$_0$_7_FPA			3.42		2.27	
pH$_0$_10_FPA			3.41		2.25	
Unaltered Fe-rich allophane*			3.50	*2.60*	*2.24*	*1.92*
pH$_0$_3_FRA*			3.47	*2.60*	*2.24*	
pH$_0$_5_FRA			3.47			
pH$_0$_7_FRA*			3.45		*2.21*	
pH$_0$_10_FRA*	*12.2*		3.45	*2.60*	*2.24*	*1.92*

*Quartz contamination from grinding in agate mortar and pestle was observed in the form of a small, sharp peak at 3.34 Å. Contamination was more common in Fe-rich samples because the Fe-rich allophane was harder than the other allophanes and required more rigorous grinding.